AD NUMBER: AD0484898
LIMITATION CHANGES
TO: Approved for public release; distribution is unlimited.
FROM: Distribution authorized to US Government Agencies and their Contractors; Administrative/Operational Use; 23 Mar 1966. Other requests shall be referred to Office of Naval Research, Arlington, VA 22203.
AUTHORITY
ONR notice dtd 27 Jul 1971

CONSIDERATION AND EVALUATION OF FACTORS INFLUENCING THE STIMULATED OPTICAL SCATTERING IN GASES

R. W. Minck, E. E. Hagenlocker, and W. G. Rado
Physics Department

March 23, 1966

SCIENTIFIC LABORATORY

Final Report to Office of Naval Research
Contract Nonr 4712(00)

Raman Laser Studies
NR 015-325

SCIENTIFIC RESEARCH STAFF

Ford
MOTOR COMPANY

ABSTRACT

In the presence of intense laser beams, the normally weak raman and brillouin scattering from materials can become stimulated. The customary theory predicts that the intensity of the scattered stokes wave grows exponentially with distance at fixed laser power. This report presents the results of numerical calculations of the gain factor for the important scattering mechanisms in several diatomic gases as functions of temperature and pressure. Competition and transitions between various stimulated processes are predicted as functions of pressure and temperature.

Some experimental data is presented to indicate that it is in general agreement with the simple theory. The experimental verification of the crossing over between processes and indications of the competition near the crossover are also presented.

I. INTRODUCTION

The following report consists of the numerical evaluation of quantities needed to predict the threshold requirements for stimulated raman (srs) and brillouin scattering (sbs) in several homonuclear diatomic gases as a function of gas pressure and temperature. Pertinent data are compiled from spectroscopic and thermodynamic studies and are included in the report. The spatial rate of gain of the stokes radiation for several strong raman lines and the brillouin line are calculated incorporating the population distributions and transition linewidths for srs and the actual compressibilities, viscosities and densities for sbs. The interactions are idealized by assuming plane wave solutions, a single undepleted monochromatic laser beam, and steady state conditions. Experimentally, deviations from the above idealizations are universally present and can have a major influence on details of the interactions. Non-ideal laser properties,[1] transient conditions,[2] self-induced filamentation,[3] competition between several processes,[4] and many other effects are being considered by other workers, and can lead to orders of magnitude change from the simplified model. Thus it is intended that this report will simply serve to indicate trends and magnitudes of effects. Comparison with existing data will be included wherever available to indicate the degree of agreement.

The raman calculations are based on a model of inelastic scattering of light from individual molecules whose motions are perturbed by collisions with neighboring molecules. Consideration of the molecular motions leads to doppler broadening, motional narrowing, and pressure broadening. At high particle density, a transition must be made to a model which

includes correlations and coupling between adjacent molecules. At very high density an optical phonon band model would be more appropriate. Calculations of stimulated brillouin scattering are made following the procedure outlined in reference (5) which assumes a continuous media and the validity of the classical Navier-Stokes equations.[6] The theory reduces to the normal mode formulism[7] at high pressures, but deviates at low pressures when the mean free path exceeds the acoustic wavelength.

II. THEORY

Stimulated raman and brillouin scattering involves the interaction of intense optical beams with excitation waves in transparent materials. To properly describe these interactions, a detailed knowledge of the wave properties are needed. Although there is a tendency to relate the raman and brillouin waves to the optical and accustic branches of the vibrational waves which occur in crystalline materials, the assignment fails in the gas phase, particularly at low pressures. The study of scattering in the gas phase thus offers an interesting opportunity to investigate inter-molecular effects as a function of particle density.

The customary derivation[8] of stimulated scattering involves a model in which a single pair of monochromatic EM plane waves are coupled to one resonant molecular wave. Under steady state conditions, the interaction can be described in terms of a nonlinear electric polarizability, resonant and third order in the electric field strength.[9] In this formulism, it can be treated systematically along with other third order effects (i.e., two photon absorption, intensity dependent index, etc.). The induced dipole moment at the stokes frequency due to a strong laser field propagating in

the z direction can be written as

$$P(\omega_s)e^{ik_s z} = \chi E(\omega_L)E^*(\omega_L)E(\omega_s)e^{ik_s z} \qquad (1)$$

where for simplicity, the polarizations of the fields are assumed parallel so that the symmetric susceptibility tensor takes on a scalar value. The interaction must conserve energy and momentum requiring that the frequencies and wave vectors for the laser, stokes, and molecular waves satisfy $\omega_m = \omega_L - \omega_s$ and $\bar{k}_m = \bar{k}_L - \bar{k}_s$.

The susceptibility χ is complex and contains both a resonant and a non-resonant part. The non-resonant term results from two photon absorptions at other frequencies and exhibits little dispersion in the region of interest. The resonant term is due to the interaction with the molecular wave and is characterized by a line strength and a linewidth. A number of such resonant terms occur due to the multiplicity of raman transitions. If these lines are resolvable under normal (spontaneous raman) spectroscopy, the influence of these nearby but weaker lines on the stimulation of the strongest line is small. Under conditions where line broadening causes the lines to overlap, one should in principle sum their complex polarizabilities. This applies in the case of the low J levels in the Q branch of O_2 and N_2 at high pressures. For purposes of the report, problems of this nature will not be considered, and only resolvable transitions will be considered.

For the strong interactions of interest here, the resonant contribution (χ^r) will dominate the non-resonant part and will be purely imaginary exactly on resonance. Writing the stokes waves as $\bar{E}(z,t) = \bar{E}(z) \exp[-i(\omega_s t - k_s z)]$ the linearized growth of its amplitude can be

written[10]

$$\frac{dE(\omega_s)}{dz} = i\frac{2\pi k_s}{\epsilon_s} P^{NL}(\omega_s)e^{-k_s z} = \frac{2\pi k_s}{\epsilon_s} |\chi^r| E(\omega_L)E^*(\omega_L)E(\omega_s) \qquad (2)$$

from which

$$\bar{E}(\omega_s) = \bar{E}_o(\omega_s) \exp(z/\ell) \quad . \qquad (3)$$

Thus the amplitude of the stokes wave grows exponentially as z/ℓ, and the power grows as $2z/\ell$. By removing the laser intensity I_L, a normalized gain factor is obtained which is characteristic of the material and the particular transition.

$$I(\omega_s) = I_o(\omega_s) \exp(gI_L z) \; . \qquad (4)$$

where $g = \frac{2}{\ell I_L} = \frac{32\pi^2 k_s \chi^r}{\epsilon_s n_L c}$.

Two important features of this interaction are that the field grows exponentially with distance and that phase matching is automatically satisfied since the dipole is induced with the proper phase which leads to growth, independent of the phase relation between the laser and the stokes waves. In fact, the stokes and laser waves need not even be collinear.[11]

The exponential growth with distance applies to both sbs and srs and has the same dependence on laser power and distance for these processes. A competition between the processes will occur and the transition with the highest gain will dominate. Since high gain is assumed (exp 30), a 10% difference in normalized gain for two processes would correspond to roughly e^3 or a factor of 20 difference in intensity between them. That the dominant process does not experimentally suppress the less likely one will be discussed in Part IV.

For raman scattering, the resonant polarizability is given by[9]

$$\chi_{raman} = \frac{N\alpha^2 L}{4\hbar\Gamma}$$

where N is the population difference between levels, α is the raman polarizability, Γ is the half linewidth in radians, and L is the local field correction factor. The lower particle density in a gas tends to be offset by a correspondingly narrower linewidth with the result that the value for the resonant polarizability varies little from low to high gas pressures.

The derivation for the polarizability for sbs in gases will be shown in detail here since it has not appeared elsewhere. Actually one expects an exact analogy to the analysis of sbs in a liquid as long as the gas can be treated as a continuous medium. At low pressures where the mean free path becomes comparable to the acoustic wavelength, the assumption of a continuum is no longer justified. However, experimental results[12] have shown that the classical Navier-Stokes theory for the propagation of sound in a continuum continues to predict the acoustic behavior of gases as accurately as any present statistical theory in this low pressure region. The derivation will thus assume a continuous media.

For a volume V whose dimensions are small compared to an acoustic wavelength so that the internal particles are in equilibrium, the conservation of mass requires that

$$-\frac{\Delta\rho}{\rho} = \frac{\Delta V}{V} = \nabla\cdot\vec{\eta}$$

where ρ is the density, V the volume, and $\vec{\eta}$ is the displacement of the surface enclosing the volume. The Lagrangian density is

$$\mathcal{L} = \tfrac{1}{2}\rho\left(\frac{\partial\vec{\eta}}{\partial t}\cdot\frac{\partial\vec{\eta}}{\partial t}\right) + P(\nabla\cdot\vec{\eta}) - \tfrac{1}{2}\rho\left(\frac{\partial P}{\partial\rho}\right)_s(\nabla\cdot\vec{\eta})^2$$

$$+ \frac{1}{8\pi c^2}\left[\epsilon_o - \rho\left(\frac{\partial\epsilon}{\partial\rho}\right)_s(\nabla\cdot\vec{\eta})\right]\left(\frac{\partial\vec{A}}{\partial t}\cdot\frac{\partial\vec{A}}{\partial t}\right) - \frac{1}{8\pi\mu}(\nabla\times\vec{A})\cdot(\nabla\times\vec{A}) \quad (5)$$

where $\left(\frac{\partial P}{\partial\rho}\right)_s$ and $\left(\frac{\partial\epsilon}{\partial\rho}\right)_s$ are the adiabatic fluctuations of pressure and dielectric constant with density, $\vec{A}$ is the vector potential associated with the electromagnetic fields in the medium, and the other symbols have their conventional meanings. The term which contains $\rho\left(\frac{\partial\epsilon}{\partial\rho}\right)_s$ expresses the photoelastic coupling between the electromagnetic waves and elastic (acoustic) waves.

Using complex half-amplitude notation, the coupled wave equations can be written in the following form:

$$\rho\frac{\partial^2\sigma^*}{\partial t^2} - \rho\left(\frac{\partial P}{\partial\rho}\right)_s\nabla^2\sigma^* + \beta\nabla^2\left(\frac{\partial\sigma^*}{\partial t}\right) = \frac{\rho\left(\frac{\partial\epsilon}{\partial\rho}\right)_s}{4\pi c^2}\nabla^2\left(\frac{\partial\vec{A}_L^*}{\partial t}\cdot\frac{\partial\vec{A}_s}{\partial t}\right) \quad (6)$$

$$\nabla^2\vec{A}_s - \frac{\mu\epsilon_c}{c^2}\frac{\partial^2\vec{A}_s}{\partial t^2} = \frac{\mu\rho\left(\frac{\partial\epsilon}{\partial\rho}\right)_s}{c^2}\sigma^*\frac{\partial^2\vec{A}_L}{\partial t^2} \quad (7)$$

where σ is the fractional change in density, $\vec{A}_L$ and $\vec{A}_s$ are the vector potentials of the laser and stokes waves, and $\beta\nabla^2\left(\frac{\partial\sigma^*}{\partial t}\right)$ represents the damping losses due to viscosity and thermal conductivity.[6] Attenuation of the stokes and laser waves in the medium has been neglected.

When $\vec{A}_L$, $\vec{A}_s$, and σ are assumed to be plane waves of the form $G(z)e^{-i(\omega t \pm kz)}$, the coupled wave equations can be linearized by neglecting the second derivative of the waves' amplitudes. When the acoustic losses are large, the terms involving the spatial derivatives of the phonon amplitude can be neglected (pseudo-equilibrium) and the equations become

$$F^* = \frac{\rho\left(\frac{\partial \epsilon}{\partial \rho}\right)_s \omega_L \omega_s k_B^2 A_L^* A_s}{4\pi c^2 \left[\rho\omega_B^2 - \rho\left(\frac{\partial P}{\partial \rho}\right)_s k_B^2 + i\beta\omega_B k_B^2\right]} \tag{8}$$

$$\frac{dA_s}{dz} = \frac{i\mu\omega_L^2 \rho\left(\frac{\partial \epsilon}{\partial \rho}\right)_s F^* A_L}{2k_s c^2} \tag{9}$$

where F, A_L, and A_s are the complex half-amplitudes of the acoustic wave, laser wave, and stokes wave; $\vec{k}_B$, $\vec{k}_L$, $\vec{k}_s$ and ω_B, ω_L, ω_s are their real wave vectors and frequencies. The expression for the power gain (g) of the stokes wave normalized per unit length per laser intensity becomes

$$g = \frac{2}{\mu I_L} = \frac{k_s \left[\rho\left(\frac{\partial \epsilon}{\partial \rho}\right)_s\right]^2 \beta \omega_B}{2cn^3 \left[\left(\rho\left(\frac{\omega_B}{k_B}\right)^2 - \rho\left(\frac{\partial P}{\partial \rho}\right)_s\right)^2 + \beta^2 \omega_B^2\right]} \tag{10}$$

In the above power gain expression, k_B is determined by the geometry of the experiment but ω_B has not yet been specified. The method of excitation requires that ω_B and k_B must both be real at every point in the interaction volume. Maximizing the gain with respect to ω_B places the following condition on the phase velocity ω_B/k_B :

$$3\left(\frac{\omega_B}{k_B}\right)^2 = v^2 - M^2 + (4v^4 - 2v^2M^2 + M^4)^{\frac{1}{2}} \tag{11}$$

where $v = \left(\left(\frac{\partial P}{\partial \rho}\right)_s\right)^{\frac{1}{2}}$ is the velocity of sound and $M = \frac{\beta k_B}{\rho}$. At high pressures this expression reduces to $\frac{\omega_B}{k_B} = v$ which is identical to the result obtained from normal mode solutions of the Navier-Stokes equations. In the limit of low densities, this relation becomes $\frac{\omega_B}{k_B} = \frac{\rho\left(\frac{\partial P}{\partial \rho}\right)_s}{\sqrt{2}\,\beta k_B}$ which shows that the maximum gain condition corresponds to a phase velocity that decreases as the density decreases. This velocity dispersion at low pressure is opposite to that predicted from normal mode solutions of the Navier-Stokes equations.

A question is raised as to the correctness of the form of the loss term employed by Trusdell[6] ($\nabla^2 \frac{\partial}{\partial t}$). All four variations of the third derivative reduce to the proper form in the low loss region, and each predicts a different behavior in the high loss case. One of the interesting possibilities is to study sbs in this region experimentally to determine which form is proper.

III. NUMERICAL EVALUATION

A. Raman

1) Energy Levels

The energy associated with various states of a homonuclear diatomic molecule is approximated by a power series expansion in the variables, n, v, J and M; the electronic and vibrational quantum numbers, the total angular momentum, and the component along a space fixed axis, respectively. For this class of molecules in the electronic ground state and not subject to perturbing electric and magnetic fields, the M levels are degenerate. The energy of the levels can then be essentially separated into two contributions--the vibrational and the rotational energy.

$$
\begin{aligned}
W(v,J) &= G(v) + F(J) \\
G(v) &= \omega_e(v+\tfrac{1}{2}) - \omega_e x_e (v+\tfrac{1}{2})^2 + \omega_e y_e (v+\tfrac{1}{2})^3 + \cdots \\
F(J) &= [B_e - \alpha_e(v+\tfrac{1}{2}) + \gamma_e(v+\tfrac{1}{2})^2 + \cdots] J(J+1) \\
&\quad - [D_e + \beta_e(v+\tfrac{1}{2}) + \delta(v+\tfrac{1}{2})^2 + \cdots] J^2(J+1)^2 \\
&\quad + H_v J^3 (J+1)^3 + \cdots
\end{aligned}
\tag{12}
$$

The rotational energy $F(J)$ of a non-rigid rotor depends slightly on the vibrational quantum number because of a variation of moments of inertia with vibrational level. The higher order coefficients (γ, δ, H) are small and have been determined for only the light molecules (i.e., H_2 and D_2). Values for the coefficients can be found in the literature for many molecules, and a convenient compilation is presented in "Spectra of Diatomic Molecules" by Herzberg.[13] The selection rules applicable to raman scattering, a two-photon process, are $\Delta v = 0$, $\Delta J = \pm 2$ or $\Delta v = \pm 1$, $\Delta J = 0, \pm 2$. Three groups of transition are formed by the selection rules $\Delta J = -2, 0, +2$ are are labeled the O, Q, and S branches, respectively. The transitions involving a change of rotational quantum number are easily resolvable since the splittings depend on the rotational constant. The pure vibrational transitions comprise the strong Q branch and are resolvable at low gas pressure because of the small vibrational correction terms (α, γ, β, δ) to the rotational constants. For the molecules considered here, the splittings in the Q branch are sufficiently large so that a mode-controlled giant pulse laser can interact with the individual lines as long as they themselves do not overlap due to pressure broadening.

The exact transition frequencies can be evaluated by eq. (12) although useful approximations are given in Table 1. The more exact values are calculated and listed for H_2, D_2, N_2 and O_2 in Tables 2 to 5.

The notation which will be used in this report to describe a raman transition between levels (v,J) and (v', J') involves the letter for the branch, subscripts for the initial and final vibrational levels, and the initial rotational level in parentheses (i.e., $S_{vv'}(J)$, $Q_{vv'}(J)$, or $O_{vv'}(J)$.).

TABLE 1

APPROXIMATE RAMAN FREQUENCIES

Type of Transition	Notation	Approximate Frequency
Pure Rotation		
Between (v=0,J)	$S_{00}(J)$	$(B_e - \frac{1}{2}\alpha_e)(4J+6)$
and (v=0,J+2)	$O_{00}(J+2)$	
Pure Vibration		
Between (v=0,J)	$Q_{01}(J)$	$\omega_e - 2\omega_e x_e + \frac{13}{4}\omega_e y_e - \alpha_e J(J+1)$
and (v=1,J)		$G(1) - G(0) - \alpha_e J(J+1)$
Combination Transitions		
Between (v=0,J)	$S_{01}(J)$	$G(1) - G(0) + B_e(4J+6) - \alpha_e(J^2+7J+9)$
and (v=1,J+2)	$O_{10}(J+2)$	
Between (v=0,J)	$O_{01}(J)$	$G(1) - G(0) - B_e(4J-2) - \alpha_e(J^2-5J+3)$
and (v=1,J-2)	$S_{10}(J-2)$	

TABLE 2

H_2 RAMAN TRANSITION FREQUENCIES IN CM^{-1}

J	$S_{00}(J)$	$Q_{01}(J)$	$S_{01}(J)$	$O_{01}(J)$
0	354.33	4161.14	4497.75	--
1	586.85	4155.22	4712.70	--
2	814.08	4143.43	4916.67	3806.81
3	1034.37	4125.85	5108.10	3568.37
4	1246.58	4102.60	5285.85	3329.35
5	1450.19	4073.73	5449.25	3091.48

Molecular Constants taken from C. H. Church[14]

ω_e	4401.60	B_e	60.8496	D_e	0.04955	$H_0 = 9.6\ 10^{-8}$
$\omega_e x_e$	121.66	α_e	3.0438	β_e	-0.00395	$H_1 = 7.9\ 10^{-8}$
$\omega_e y_e$	0.88	γ_e	0.0396*	δ	.00087	$H_2 = 7.0\ 10^{-8}$

*Value taken as half that listed in thesis.

TABLE 3

D_2 RAMAN TRANSITION FREQUENCIES IN CM^{-1}

J	$S_{00}(J)$	$Q_{01}(J)$	$S_{01}(J)$	$O_{01}(J)$
0	179.04	2993.49	3166.21	--
1	297.52	2991.38	3278.39	--
2	414.71	2987.17	3387.16	2814.45
3	530.09	2980.87	3492.03	2693.87
4	643.18	2972.45	3592.49	2572.46
5	753.41	2961.93	3687.99	2450.77
6	860.34	2949.30	3778.08	2329.27

Molecular Constants taken from C. H. Church[14]

$\omega_e = 3112.81$ $\quad \beta_e = 30.434$ $\quad D_e = 0.01085$

$\omega_e x_e = 59.66$ $\quad \alpha_e = 1.061$ $\quad H = 10^{-8}$

$\gamma_e = 0.0045$*

*Value taken as half that listed in thesis.

TABLE 4

N_2 RAMAN TRANSITION FREQUENCIES IN CM^{-1}

J	$S_{00}(J)$	$Q_{01}(J)$	$S_{01}(J)$	$O_{01}(J)$
0	12.0042	2330.712	2342.604	--
1	20.0070	2330.674	2350.494	--
2	28.0098	2330.600	2358.347	2318.708
3	36.0126	2330.488	2366.162	2310.668
4	44.015	2330.338	2373.941	2302.591
5	52.018	2330.151	2381.682	2294.476
6	60.020	2329.927	2389.385	2286.324
7	68.023	2329.665	2397.052	2278.134
8	76.026	2329.366	2404.672	2269.907
9	84.029	2329.029	2412.272	2261.643
10	92.032	2328.655	2419.827	2253.341
11	100.035	2328.244		

Molecular Constants taken from Herzberg[13]

ω_e	2359.61	B_e	2.010
$\omega_e x_e$	14.456	α_e	0.0187
$\omega_e y_e$	0.00751		

TABLE 5

O_2 RAMAN TRANSITION FREQUENCIES IN CM^{-1}

J	$S_{00}(J)$	$Q_{01}(J)$	$S_{01}(J)$	$O_{01}(J)$
1	14.38	1556.36	1570.58	--
3	25.88	1556.20	1581.79	1541.98
5	37.37	1555.92	1592.87	1530.33
7	48.86	1555.51	1603.83	1518.55
9	60.34	1554.97	1614.64	1506.65
11	71.81	1554.31	1625.33	1494.63
13	83.27	1553.52	1635.87	1482.50
15	94.71	1552.60	1646.27	1470.25

Molecular Constants taken from Herzberg[13]

ω_e	1580.361	B_e	1.4456	D_e	4.957×10^{-6}
$\omega_e x_e$	12.073	α_e	0.01579	β_e	-0.088×10^{-6}
$\omega_e y_e$	0.0546				
$\omega_e z_e$	-0.00143				

2) Density of States and Population Distributions

The density of states has a (2J+1) factor arising from the M-degeneracy of the J^{th} rotational level, and an (I+1)/I nuclear degeneracy factor from the nuclear spin. The nuclear factor, which alternates for the even- and odd-numbered J levels, arises from symmetry requirements on the total wave function of the molecule, and favors even-numbered J values for I = 1 (D_2,N_2^{14}), and odd-numbered J values for I = 1/2 (H_2). For I = 0, (O_2^{16}) the infinite ratio excludes the even-numbered J levels.

Because the vibrational energy is much greater than kT, the initial populations are distributed among the rotational levels in the ground vibrational state. Using the known energy levels, the Boltzmann factor can be calculated. The population distribution among the J levels for various temperatures from 75°K to 500°K have been calculated and are presented in Tables 6 through 9.

TABLE 6

POPULATION DISTRIBUTION $N(J)/N_{Total}$ AS A FUNCTION OF TEMPERATURE - H_2

J	M Degen.	Nuclear Degen.	25°	37.5°	50°	62.5°	75°	100°	125°	150°	200°	250°	300°	400°	500°
0	1	1	.9919	.9235	.7892	.6494	.5352	.3875	.3039	.2532	.1927	.1572	.1335	.1025	.0833
1	3	3	.0080	.0764	.2107	.3506	.4624	.6034	.6717	.7063	.7186	.6996	.6675	.5952	.5283
2	5	1					.0024	.0099	.0227	.0367	.0839	.0951	.1141	.1367	.1447
3	7	3							.0012	.0048	.0158	.0474	.0812	.1506	.2083
4	9	1										.0011	.0030	.0106	.0214
5	11	3											.0005	.0040	.0124
6	13	1													.0058
7	15	3													.0021

TABLE 7

POPULATION DISTRIBUTION $N(J)/N_{Total}$ AS A FUNCTION OF TEMPERATURE - D_2

J	M Degen.	Nuclear Degen.	25°	37.5°	50°	75°	100°	125°	150°	200°	250°	300°	350°	500°
0	1	2	.9523	.8621	.7692	.6079	.4489	.4056	.3454	.2666	.2166	.1821	.1575	.1126
1	3	1	.0476	.1318	.2077	.2917	.3129	.3062	.2936	.2599	.2307	.2049	.1850	.1424
2	5	2		.0043	.0231	.0973	.1882	.2596	.3108	.3666	.3878	.3870	.3779	.3372
3	7	1				.0030	.0097	.0243	.0379	.0719	.0964	.1147	.1259	.1396
4	9	2						.0040	.0121	.0319	.0606	.0928	.1204	.1813
5	11	1								.0026	.0065	.0127	.0212	.0467
6	13	2										.0054	.0110	.0298
7	15	1											.0008	.0062
8	17	2												.0039

TABLE 8

POPULATION DISTRIBUTION $N(J)/N_{Total}$ AS A FUNCTION OF TEMPERATURE - N_2

J	M Degen.	Nuclear Degen.	75°	100°	150°	200°	250°	300°	350°
0	1	2	.0501	.0378	.0253	.0189	.0152	.0126	.0109
1	3	1	.0697	.0537	.0365	.0277	.0222	.0186	.0160
2	5	2	.1997	.1594	.1126	.0871	.0710	.0600	.0518
3	7	1	.1114	.0939	.0703	.0560	.0464	.0396	.0346
4	9	2	.2100	.1919	.1549	.1282	.1089	.0942	.0833
5	11	1	.0883	.0884	.0785	.0679	.0594	.0525	.0468
6	13	2	.1317	.1478	.1477	.1353	.1223	.1098	.1005
7	15	1	.0439	.0572	.0645	.0638	.0599	.0558	.0516
8	17	2	.0554	.0822	.1089	.1151	.1135	.1087	.1023
9	19	1	.0158	.0268	.0434	.0496	.0516	.0513	.0497
10	21	2	.0158	.0342	.0647	.0831	.0907	.0932	.0933
11	23	1	.0037	.0100	.0236	.0331	.0385	.0414	.0427
12	25	2	.0032	.0103	.0328	.0517	.0643	.0723	.0765
13	27	1	.0007	.0028	.0106	.0189	.0255	.0303	.0334
14	29	2		.0024	.0135	.0275	.0397	.0497	.0572
15	31	1		.0005	.0040	.0090	.0154	.0198	.0238
16	33	2			.0046	.0125	.0226	.0314	.0392
17	35	1			.0012	.0043	.0079	.0119	.0156
18	37	2			.0016	.0053	.0111	.0183	.0249
19	39	1				.0015	.0039	.0066	.0095
20	41	2				.0018	.0051	.0096	.0147
21	43	1				.0004	.0016	.0034	.0054
22	45	2					.0021	.0046	.0078
23	47	1					.0006	.0015	.0028
24	49	2						.0021	.0040
25	51	1						.0002	.0005

TABLE 9

POPULATION DISTRIBUTION $N(J)/N_{Total}$ AS A FUNCTION OF TEMPERATURE - O_2

J	M Degen.	75°	100°	150°	200°	250°	300°	350°
1	3	.1565	.1194	.0811	.0610	.0490	.0407	.0351
3	7	.2767	.2255	.1620	.1278	.1054	.0885	.0772
5	11	.2634	.2437	.2012	.1673	.1443	.1213	.1093
7	15	.1752	.1939	.1912	.1731	.1560	.1396	.1277
9	19	.0854	.1194	.1511	.1538	.1488	.1396	.1325
11	23	.0317	.0609	.1023	.1209	.1270	.1265	.12499
13	27	.00893	.0259	.0593	.08405	.0988	.1048	.10872
15	31	.00209	.00812	.03001	.05541	.0695	.08006	.08839
17	35		.00244	.01361	.02967	.0449	.05750	.06725
19	39		.00058	.00542	.01535	.02727	.03796	.04812
21	43			.00191	.00713	.01505	.02366	.03267
23	47			.00058	.00324	.00782	.01362	.02067
25	51				.00116	.00347	.00770	.00719
27	55					.00164	.00393	.00393
29	59					.00068	.00210	.00202
31	63						.00085	.000956
33	67						.00037	.000456

3) Line Strength

The raman polarizability is the matrix element connecting an initial (v,J,M) state to its final (v′,J′,M′) state and exists because of the variation of polarizability with nuclear coordinate. Because the M levels are degenerate for these diatomic gases, the individual transitions cannot be resolved. Thus, the spontaneously measured polarizability between J states is the sum of the (assumed incoherent) polarizabilities for all the allowed transitions $\Delta M = 0, \pm 1, \pm 2$ from each M state in the initial J level. It is commonly assumed that the polarizability is independent of M so that the value of polarizability attributed to an individual M level is the average value.

The symmetry of a diatomic molecule produces a different polarizability along the internuclear axis ($\alpha_{\parallel}$) than perpendicular to it ($\alpha_{\perp}$). The polarizability is decomposed into an isotropic term $\alpha = 1/3\ (\alpha_{\parallel} + 2\alpha_{\perp})$ and an anisotropic term $\gamma = (\alpha_{\parallel} - \alpha_{\perp})$.

As a result of this anisotropy, radiation can be scattered in a polarization perpendicular to the incident field, involving a $\Delta M = \pm 1$ transition. Radiation scattered parallel to the incident field occurs for $\Delta M = 0$, and involves primarily the isotropic polarizability. By averaging over the random orientations of the molecule in space and summing over the M levels, the transition intensities (polarizabilities squared) shown in Table 10 are obtained for linearly polarized incident light ($\Delta M = 0, \pm 1$). The notations $(S_J^{\Delta J})_{\parallel,\perp}^{v,v'}$, represents the intensities of light scattered from the initial (v,J) level to the (v′,J+ΔJ) level and polarized either parallel or perpendicular to the incident field.

TABLE 10

SCATTERING INTENSITY

$$(S_J^{\Delta J})_{\parallel,\perp}^{VV'}$$

Q branch $$(S_J^0)_{\parallel}^{01} = (\alpha_{01})^2 + \frac{4}{45}\,\frac{J(J+1)}{(2J-1)(2J+3)}\,(\gamma_{01})^2$$

$$(S_J^0)_{\perp}^{01} = \frac{1}{15}\,\frac{J(J+1)}{(2J-1)(2J+3)}\,(\gamma_{01})^2$$

S branch $$(S_J^{+2})_{\parallel}^{VV'} = \frac{2}{15}\,\frac{(J+1)(J+2)}{(2J+1)(2J+3)}\,(\gamma_{VV'})^2$$

$$(S_J^{+2})_{\perp}^{VV'} = \frac{1}{10}\,\frac{(J+1)(J+2)}{(2J+1)(2J+3)}\,(\gamma_{VV'})^2$$

O branch $$(S_J^{-2})_{\parallel}^{VV'} = \frac{2}{15}\,\frac{J(J-1)}{(2J-1)(2J+1)}\,(\gamma_{VV'})^2$$

$$(S_J^{-2})_{\perp}^{VV'} = \frac{1}{10}\,\frac{J(J-1)}{(2J-1)(2J+1)}\,(\gamma_{VV'})^2$$

The transitions with $\Delta M = \pm 2$ involve the scattering of circularly polarized light and are generally of less interest. This case has been considered elsewhere[9] and leads to interesting effects for rotational transitions, but has negligible effect on the vibrational line strengths.

When the upper level is initially populated, the observed line strength will involve the difference in populations of the M states in the initial and final (v,J) levels. This will in general be applicable for rotational transitions, but not for vibrational ones since $h\omega \gg kT$ for these. The population difference is given simply by the Boltzmann factor since the nuclear factor is common to both the initial and final levels. Its value can also be written in terms of the populations in the (v,J) levels and the M-degeneracy factor

$$\Delta N_M = \frac{N(v,J)}{2J+1} - \frac{N(v',J')}{2J'+1}$$

so that the observable transition probability, summed over all initial M levels becomes

$$\Delta N_J \, (S_J^{\Delta J})_{\parallel,\perp}^{vv'} = (2J+1)\, \Delta N_M \, (S_J^{\Delta J})_{\parallel,\perp}^{vv'}$$

$$= \left[N(v,J) - \frac{2J+1}{2J'+1} N(v',J')\right] (S_J^{\Delta J})_{\parallel,\perp}^{vv'}$$

The calculations of the observable line strengths, incorporating the temperature variation of the population distributions among the molecular levels and the appropriate transitions intensities, yield the results shown in Figures 1-4 for the several gases under study.

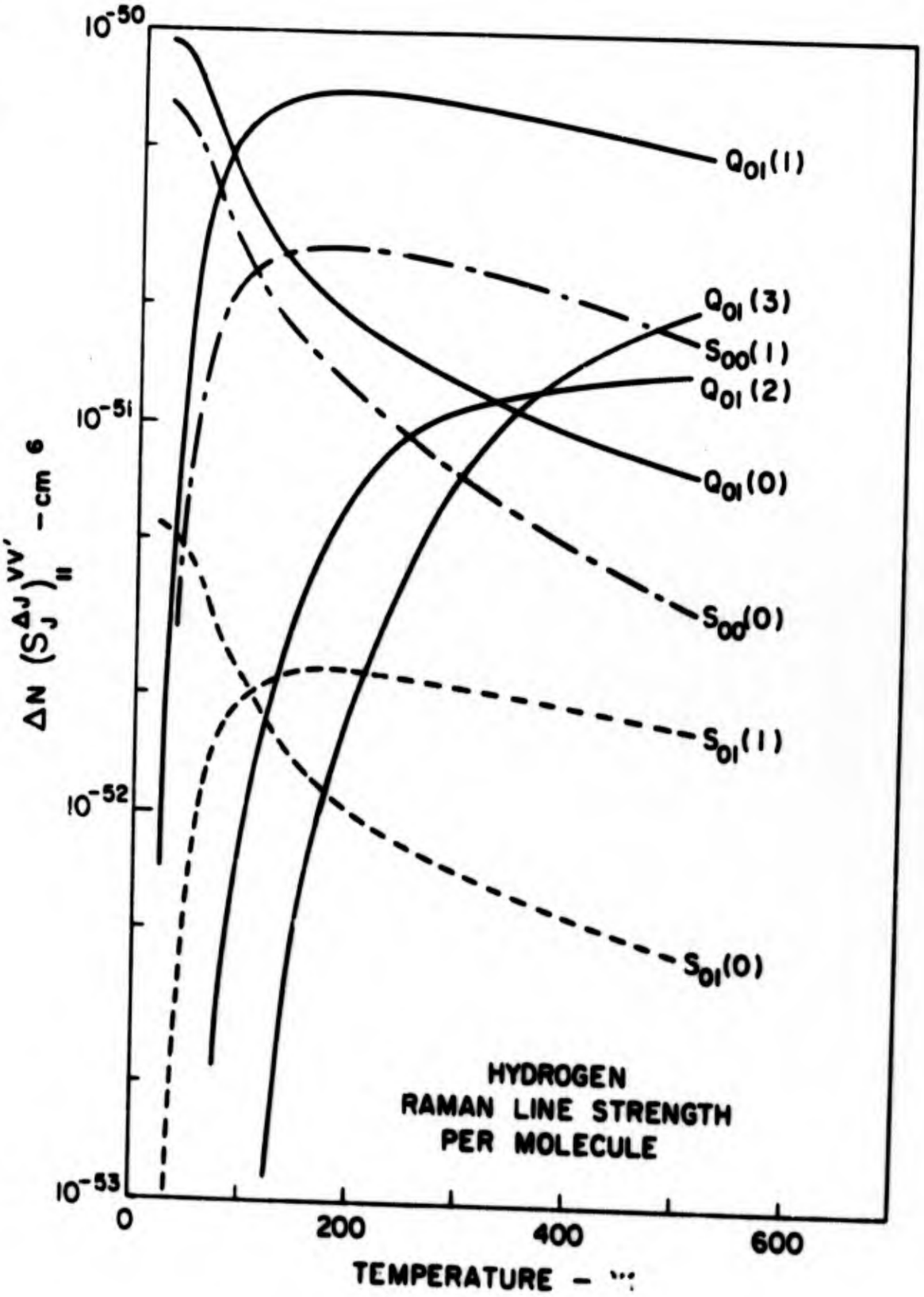
10^{-50}
10^{-51}
10^{-52}
10^{-53}
$\Delta N\ (S_J^{\Delta J})_{II}^{VV'}$ - cm 6
$Q_{01}(1)$
$Q_{01}(3)$
$S_{00}(1)$
$Q_{01}(2)$
$Q_{01}(0)$
$S_{00}(0)$
$S_{01}(1)$
$S_{01}(0)$
HYDROGEN
RAMAN LINE STRENGTH
PER MOLECULE
0
200
400
600
TEMPERATURE - °K

FIG. 1

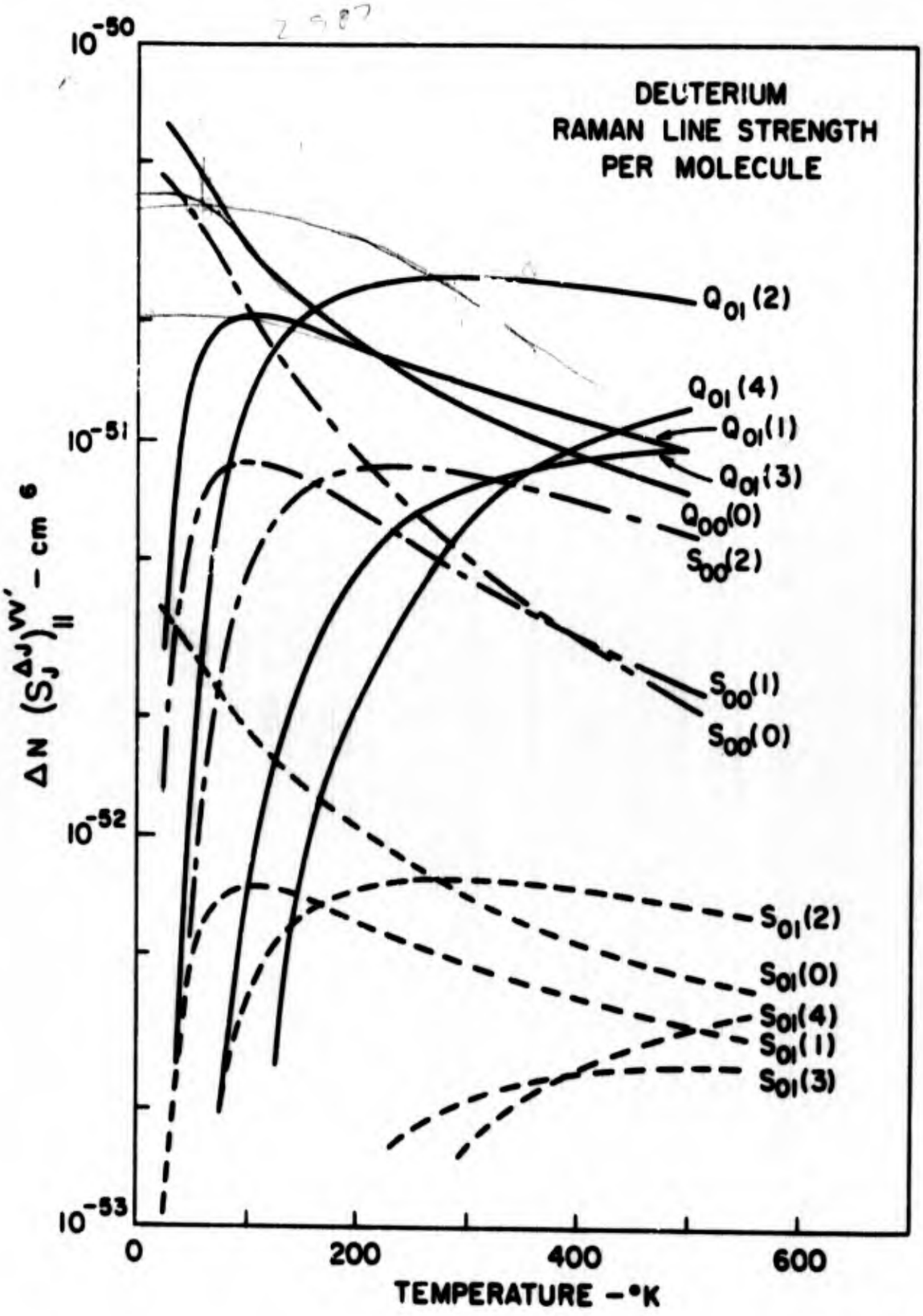
DEUTERIUM
RAMAN LINE STRENGTH
PER MOLECULE
10^{-50}
10^{-51}
10^{-52}
10^{-53}
$\Delta N\ (S_J^{\Delta J})_{II}^{VV'} - cm^6$
$Q_{01}(2)$
$Q_{01}(4)$
$Q_{01}(1)$
$Q_{01}(3)$
$Q_{00}(0)$
$S_{00}(2)$
$S_{00}(1)$
$S_{00}(0)$
$S_{01}(2)$
$S_{01}(0)$
$S_{01}(4)$
$S_{01}(1)$
$S_{01}(3)$
0
200
400
600
TEMPERATURE - °K

FIG. 2

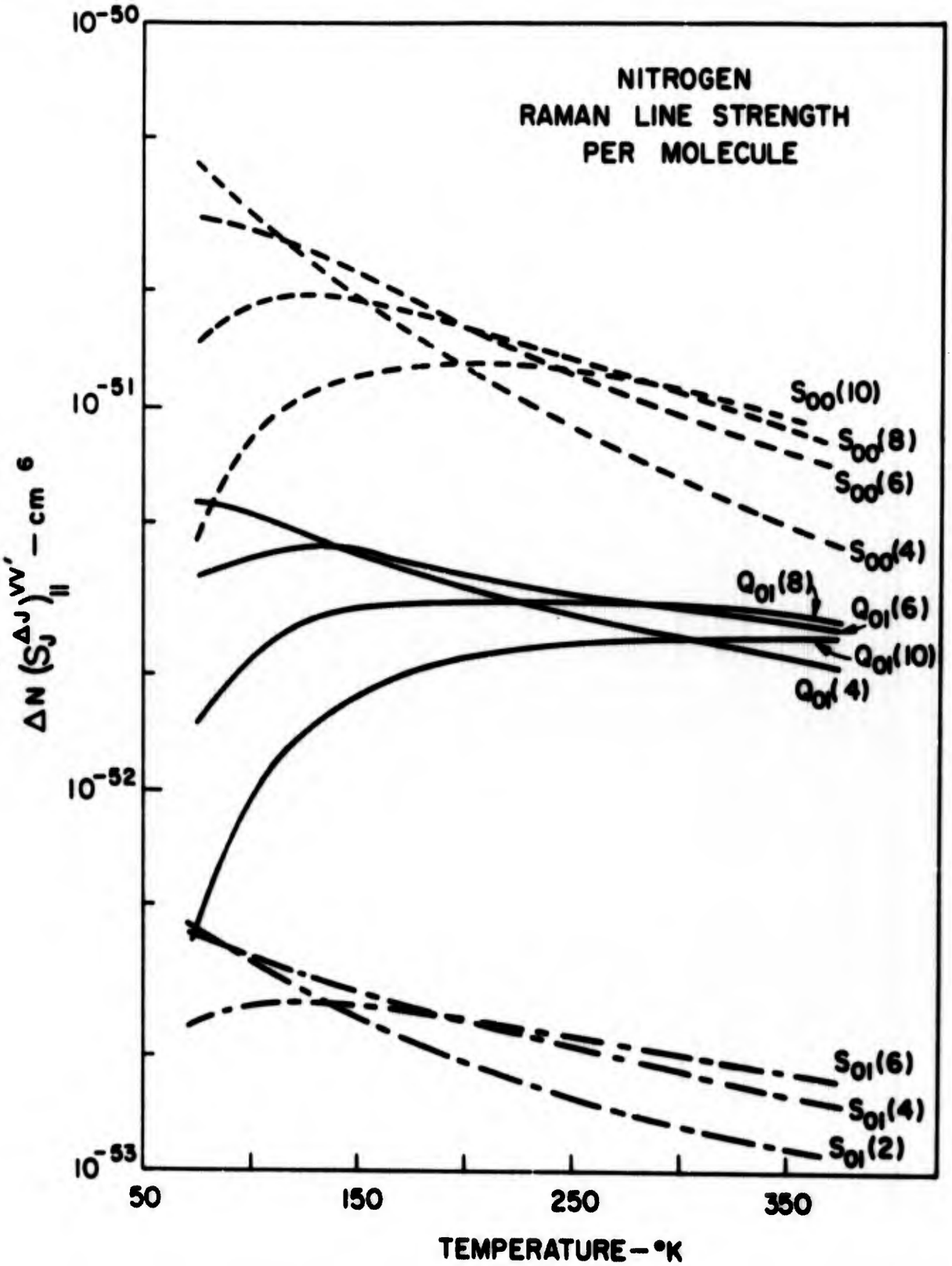
NITROGEN
RAMAN LINE STRENGTH
PER MOLECULE
10^{-50}
10^{-51}
10^{-52}
10^{-53}
$\Delta N\,(S_J^{\Delta J})_{ll}^{vv'}$ — cm^6
$S_{00}(10)$
$S_{00}(8)$
$S_{00}(6)$
$S_{00}(4)$
$Q_{01}(8)$
$Q_{01}(6)$
$Q_{01}(10)$
$Q_{01}(4)$
$S_{01}(6)$
$S_{01}(4)$
$S_{01}(2)$
50
150
250
350
TEMPERATURE — °K

FIG. 3

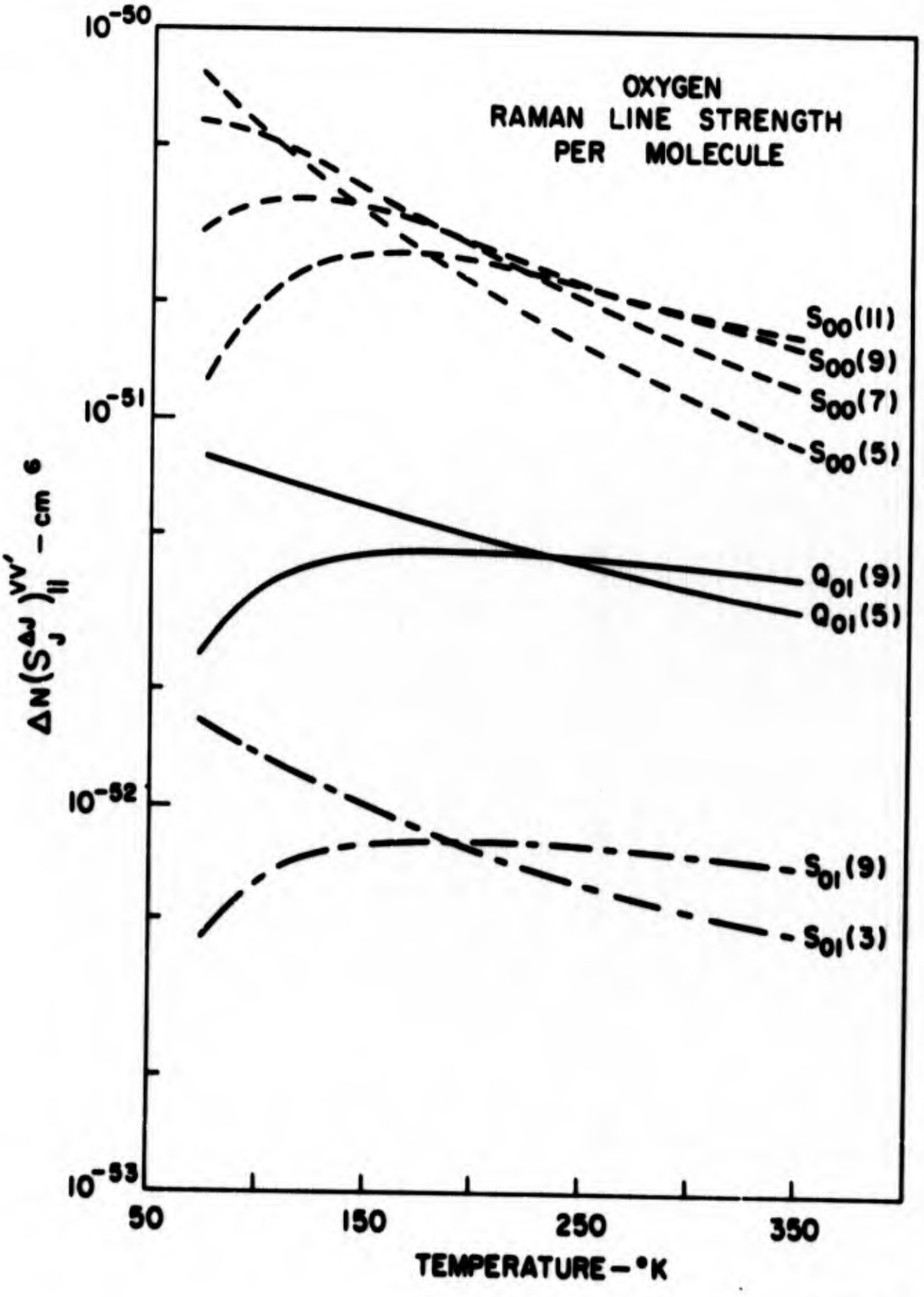
OXYGEN
RAMAN LINE STRENGTH
PER MOLECULE
10^{-50}
10^{-51}
10^{-52}
10^{-53}
$\Delta N(S_J^{\Delta\omega})_{11}^{VV'}$ – cm^6
$S_{00}(11)$
$S_{00}(9)$
$S_{00}(7)$
$S_{00}(5)$
$Q_{01}(9)$
$Q_{01}(5)$
$S_{01}(9)$
$S_{01}(3)$
50
150
250
350
TEMPERATURE – °K

FIG. 4

4) Evaluation of Line Shape Factor

The shape of spectral lines emitted by an excited atom is determined simultaneously by the perturbing influence of neighboring particles, by thermal motion of the emitter itself, and by its natural radiative lifetime. Since a raman excitation in symmetric molecules is dipolar forbidden, the natural lifetime is enormous, and can be neglected compared to the two other factors which determine the transition's line shape. These two processes (pressure broadening and doppler effect) are normally treated separately following well known analyses to yield line shapes given by

$$I(\omega-\omega') = \frac{1/\tau_L}{(\omega-\omega')^2 + (1/\tau_L)^2} \qquad (13)$$

and

$$I(\omega-\omega') = \exp\left[-(mc^2/2kT\omega'^2)\,(\omega-\omega')^2\right] \qquad (14)$$

where $\tau_L = (nQv)^{-1}$ is the mean lifetime between collisions which interrupt the radiative process, n is the density of perturbers, v their mean velocity, and Q the collision cross section; and where ω is the observed angular frequency and ω' is the undisturbed frequency. The other symbols have their conventional meanings.

To combine the two distributions for a radiating atom, a folding process known as the Voight integral is employed in which each elementary component of distribution (13) is assumed to be broadened in accordance with (14).

The procedure fails in the case of raman scattering because in general the scattering cross section for raman processes (Q_r) is less than for translational collisions (Q_t). That is, the molecule may undergo one

or more translational collisions without losing phase coherence of its vibrational or rotational state. Since this is true, the description of molecular motion during the lifetime of a raman excitation cannot be adequately described by a Maxwellian velocity distribution.

The general problem of a perturbed radiator was attacked by Dicke,[15] and in more detail by Galatry.[16] The formulism used is to calculate the Fourier transform, hence the power spectrum, of the emitted energy by writing the molecular motion as $x(t)$ and the phase shift perturbations as $\phi(t)$. The resulting lineshape is given by

$$I(\omega-\omega') = \frac{1}{2\pi}\iint e^{i(\omega-\omega')(t'-t)} \exp\left\{-i\frac{2\pi}{\lambda}[x(t')-x(t)] + i[\phi(t') - \phi(t)]\right\} dt\, dt' \qquad (15)$$

Assuming ergodicity to hold, the time integral can be replaced by an ensemble average. The description of the correlation functions $\Delta x(\tau) = x(t+\tau) - x(t)$ and $\Delta\phi(\tau) = \phi(t+\tau) - \phi(t)$ are the essential steps in the calculations. Dicke assumed that the motion was describable by the diffusion equation. Such a continuum description does not properly treat the initial period during which the discreteness of the individual steps of the molecular motion is the dominant characteristic. When the distances involved in this period become comparable to a wavelength, that is, when the mean free path is comparable to a (raman transition) wavelength, a more detailed treatment is required. Galatry employed a more elaborate position correlation function (due Chandrasekhar[17]) to obtain a solution which applied to all pressures.

The phase correlation function $\{i\Delta\phi(\tau)\}$ can be reduced to $\left\{ \frac{\tau}{\tau_L} [-(1-A') - iB'] \right\}$ where τ_L is the mean free time between the Poisson distributed collisions which disturb the phase, and

$$A' + iB' = \int_0^{2\pi} \exp(i\Delta\phi)\, p(\Delta\phi)\, d(\Delta\phi) \qquad (16)$$

The factor $(1-A')/\tau_L$ is responsible for the pressure broadening (collision limited lifetime) and is taken proportional to the collision frequency. B'/τ_L represents the shift of line center due to pressure. Lacking detailed information on the probability distribution of the phase shift for the raman process, equation (16) is evaluated in terms of the experimental data for pressure broadening and frequency shifts.

The expression for line shape becomes

$$I(\omega-\omega') = \frac{1}{\pi} \mathrm{Re} \int_0^{\infty} e^{i(\omega-\omega')\tau} F(\tau)\, d\tau$$

where

$$F(\tau) = \exp\left\{ - \frac{kT}{m\beta^2(\lambda'/2\pi)^2} [\beta\tau - 1 + \exp(-\beta\tau)] \right. \qquad (17)$$

$$\left. - \left[\frac{(1-A')}{\tau_L} + \frac{iB'}{\tau_L} \right] \tau \right\}$$

where $\beta = \frac{kT}{mD}$ is the coefficient of dynamical friction

D is the diffusion constant

λ' is the wavelength corresponding to the raman transition

The solutions so obtained flow smoothly from the low pressure limit of doppler effect, through a motional narrowing region, into the pressure broadened region at high pressures.

The physical interpretation of these regions can be made as follows: The doppler broadened region corresponds to a pressure range in which the mean free path exceeds a wavelength. Under these conditions the doppler shift corresponding to the individual particle's velocity can be resolved. The distribution of velocities is assumed Maxwellian for this region. In the motional narrowing region the mean free path is somewhat less than a wavelength while the raman phase coherence is maintained over many collisions. The effective velocity of the molecule is less than thermal because of the averaging nature of diffusion-like motion. The averaging process is effective until either limited by lifetime or until the molecule moves a wavelength. The linewidth continues to narrow with increasing pressure because more collisions and a longer time are required for the traversal of a wavelength. In the pressure broadening region the mean free path is sufficiently small such that the total length diffused during its lifetime introduces negligible phase shift, compared to the uncertainty arising from its finite lifetime.

Because raman scattering involves both an incident and a scattered photon, the doppler shift and the motional narrowing must be modified to account for the geometric factors involved. If the scattered radiation is observed at an angle α from the forward direction of the incident beam, then the effective wave vector upon which the particle velocity acts is given by

$$k_{eff} = \frac{2\pi}{\lambda_{eff}} = \frac{1}{c}\left[4\omega_o^2 \sin^2\frac{\alpha}{2} - 4\omega_o\omega_m \sin^2\frac{\alpha}{2} + \omega_m^2\right]^{\frac{1}{2}} \qquad (18)$$

where ω_o is the angular frequency of the incident beam

ω_m is the angular frequency of the raman transition.

Thus in the forward direction, the doppler width is proportional to the difference between the incident and scattered frequencies (i.e., the raman frequency) which can be very small for pure rotational transitions. For scattering in the reverse direction, the doppler width is proportional to the sum of the two photons (i.e., $\omega_o + (\omega_o - \omega_m) = 2\omega_o - \omega_m$).

Although the intensity at the line center can be simply calculated by this formulism and is the term of interest for computing raman gain for a monochromatic laser, the detailed line shapes involve tedious calculations except in either the low or high pressure limits. To give an indication whether the laser linewidth satisfies the assumption that it is narrow compared to that of the transition, one can calculate the width of an equivalent Lorentian line which would have the same peak value as does Eq. (17). The equivalent radian half-linewidth $\Gamma_{eq.} = \frac{1}{\pi\Pi(0)}$ is converted to $\Delta\nu_R$, the full width at half amplitude in cm^{-1}, for the dominant transitions. The temperature and pressure dependence of linewidth are shown in Figures 5 to 11. The extent of the motionally narrowed region depends on the ratio of Q_t/Q_r -- i.e., the number of collisions that can be experienced before loss of phase. When the number of allowable collisions becomes large, the distance moved increases slowly so that the average velocity is greatly reduced, narrowing the line. This is true for the $Q_{01}(J)$ lines in hydrogen and to a lesser extent for the rotational lines $S_{01}(J)$ in hydrogen and the $Q_{01}(J)$ lines in N_2 and O_2. For the rotational lines in N_2 and O_2, nearly every translational collisions destroys the raman phase. Thus the calculations reduce back to the Voight integral.

Details of the evaluation of the intensity at line center are now considered. The phase shift coefficient B' is assumed to be zero and the term

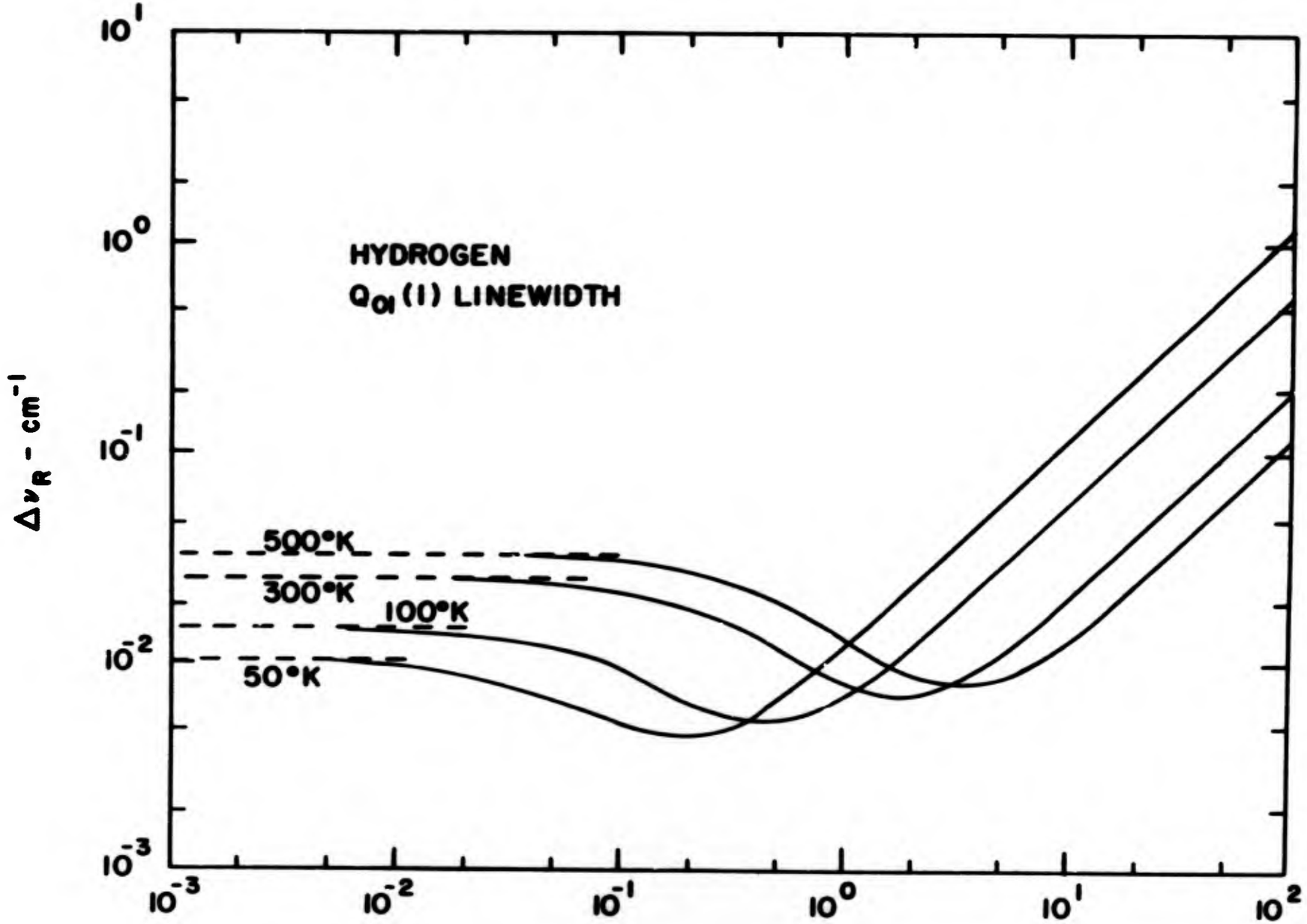
HYDROGEN
$Q_{01}(1)$ LINEWIDTH
500°K
300°K
100°K
50°K
$\Delta\nu_R$ - cm^{-1}
PRESSURE - ATM
10^{1}
10^{0}
10^{-1}
10^{-2}
10^{-3}
10^{-3}
10^{-2}
10^{-1}
10^{0}
10^{1}
10^{2}

FIG.5

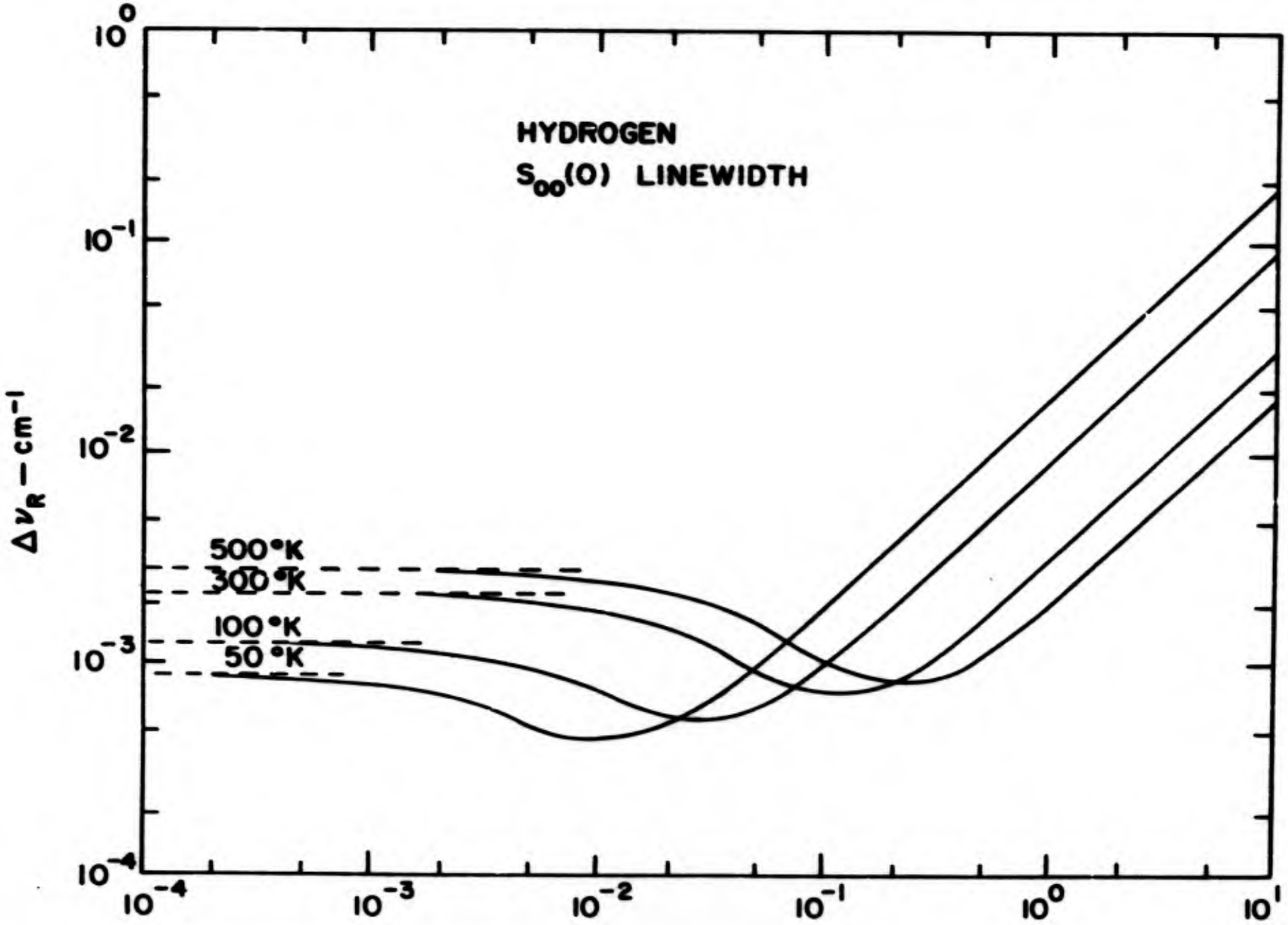
HYDROGEN
$S_{00}(0)$ LINEWIDTH
$\Delta\nu_R$ — cm^{-1}
500°K
300°K
100°K
50°K
10^0
10^{-1}
10^{-2}
10^{-3}
10^{-4}
10^{-4}
10^{-3}
10^{-2}
10^{-1}
10^0
10^1
PRESSURE — ATM.

FIG. 6

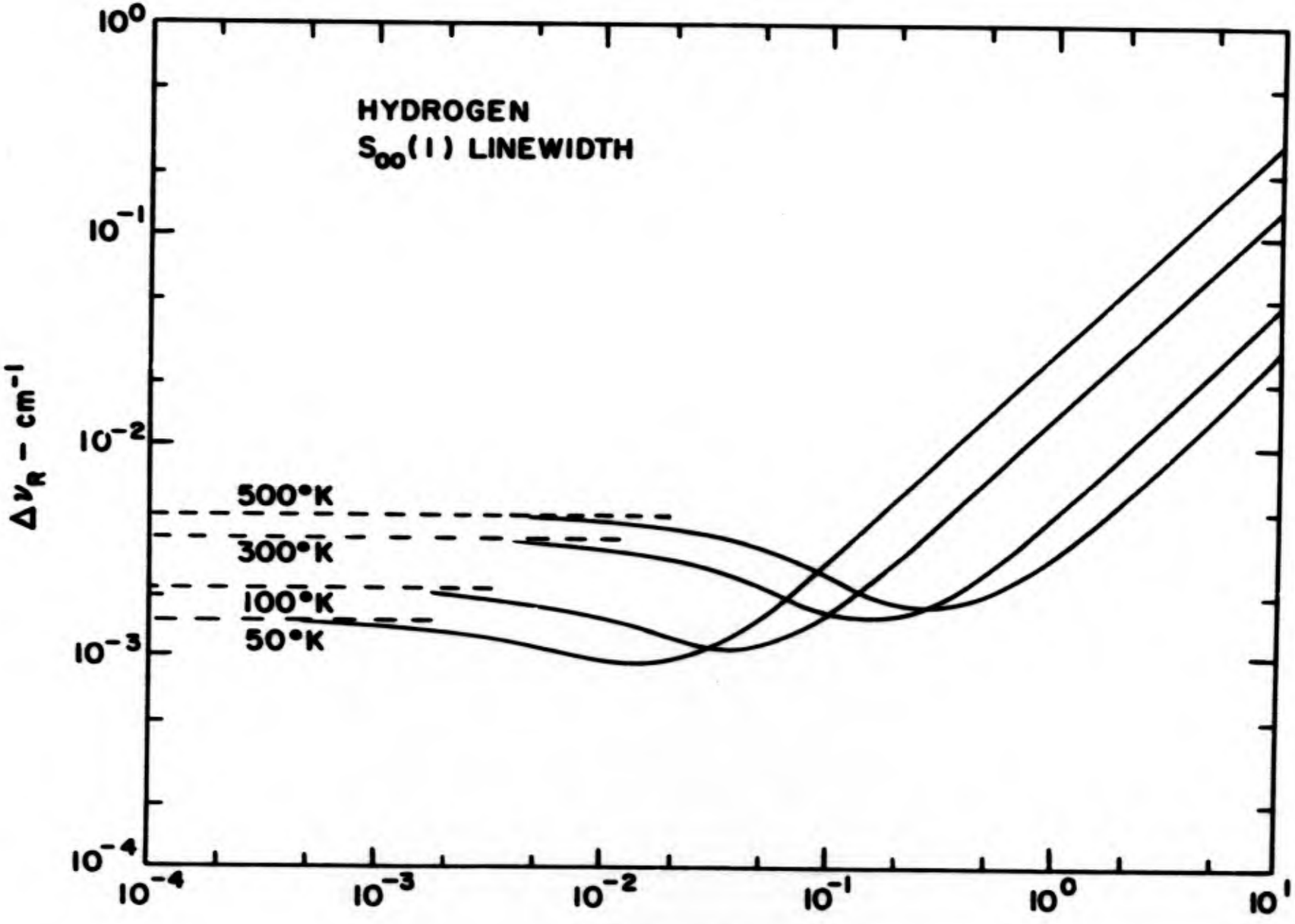
HYDROGEN
$S_{00}(1)$ LINEWIDTH
$\Delta\nu_R - cm^{-1}$
10^0
10^{-1}
10^{-2}
10^{-3}
10^{-4}
500°K
300°K
100°K
50°K
10^{-4}
10^{-3}
10^{-2}
10^{-1}
10^0
10^1
PRESSURE – ATM.

FIG. 7

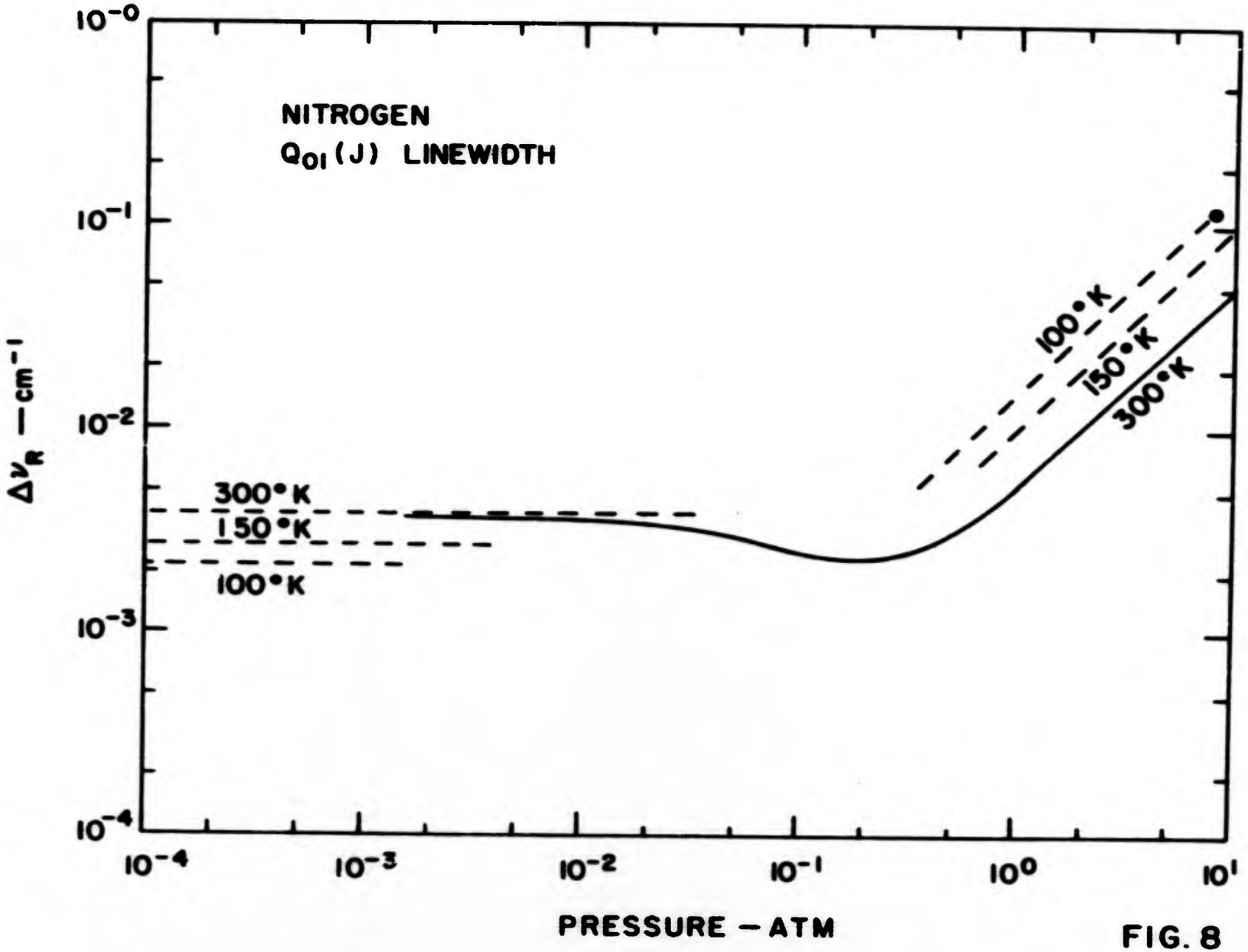
NITROGEN
$Q_{01}(J)$ LINEWIDTH
10^{-0}
10^{-1}
10^{-2}
10^{-3}
10^{-4}
$\Delta\nu_R$ — cm^{-1}
300°K
150°K
100°K
100°K
150°K
300°K
10^{-4}
10^{-3}
10^{-2}
10^{-1}
10^{0}
10^{1}
PRESSURE — ATM

FIG. 8

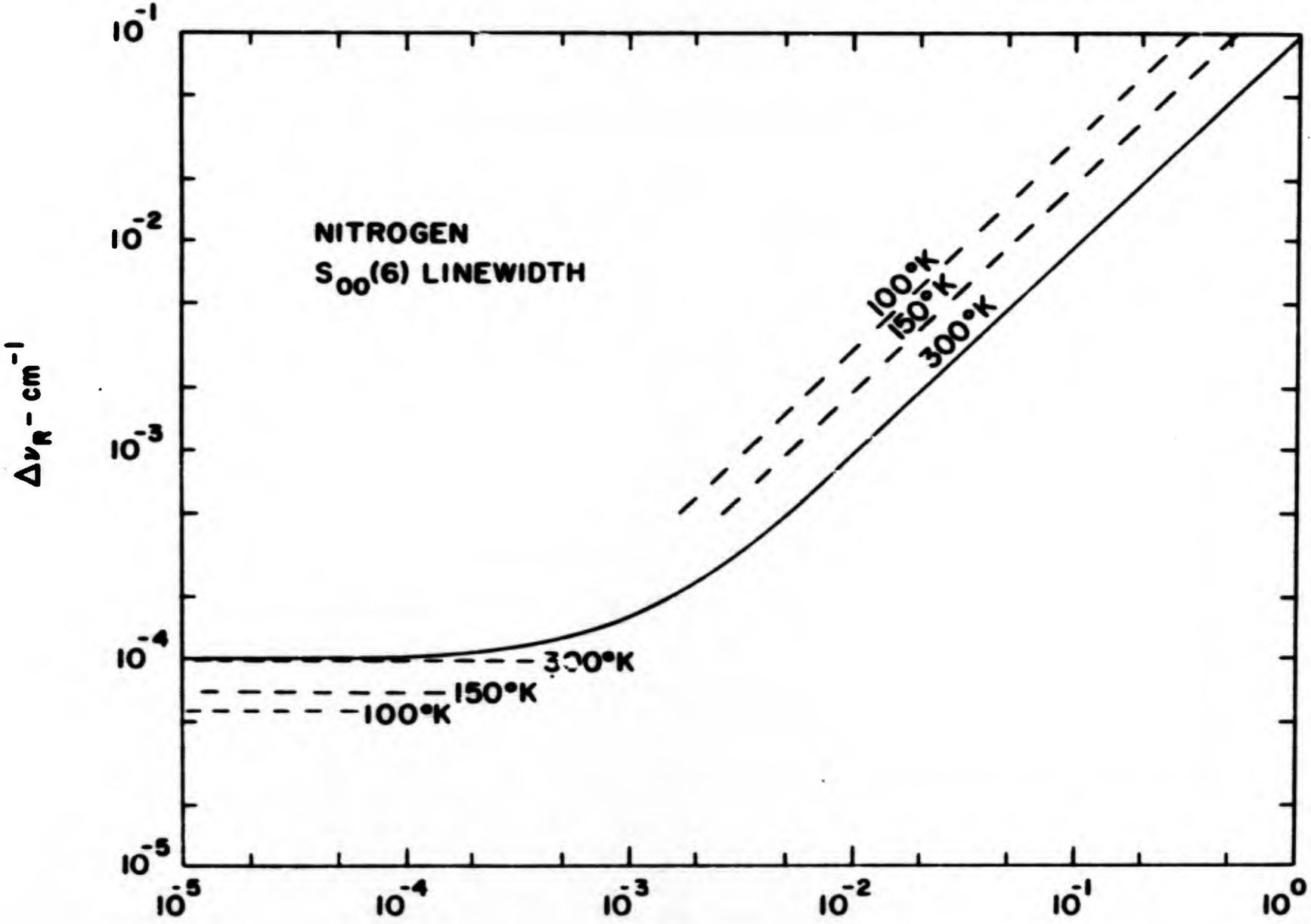
NITROGEN
$S_{00}(6)$ LINEWIDTH
100°K
150°K
300°K
300°K
150°K
100°K
$\Delta\nu_R$ - cm^{-1}
PRESSURE - ATM
10^{-1}
10^{-2}
10^{-3}
10^{-4}
10^{-5}
10^{0}

FIG. 9

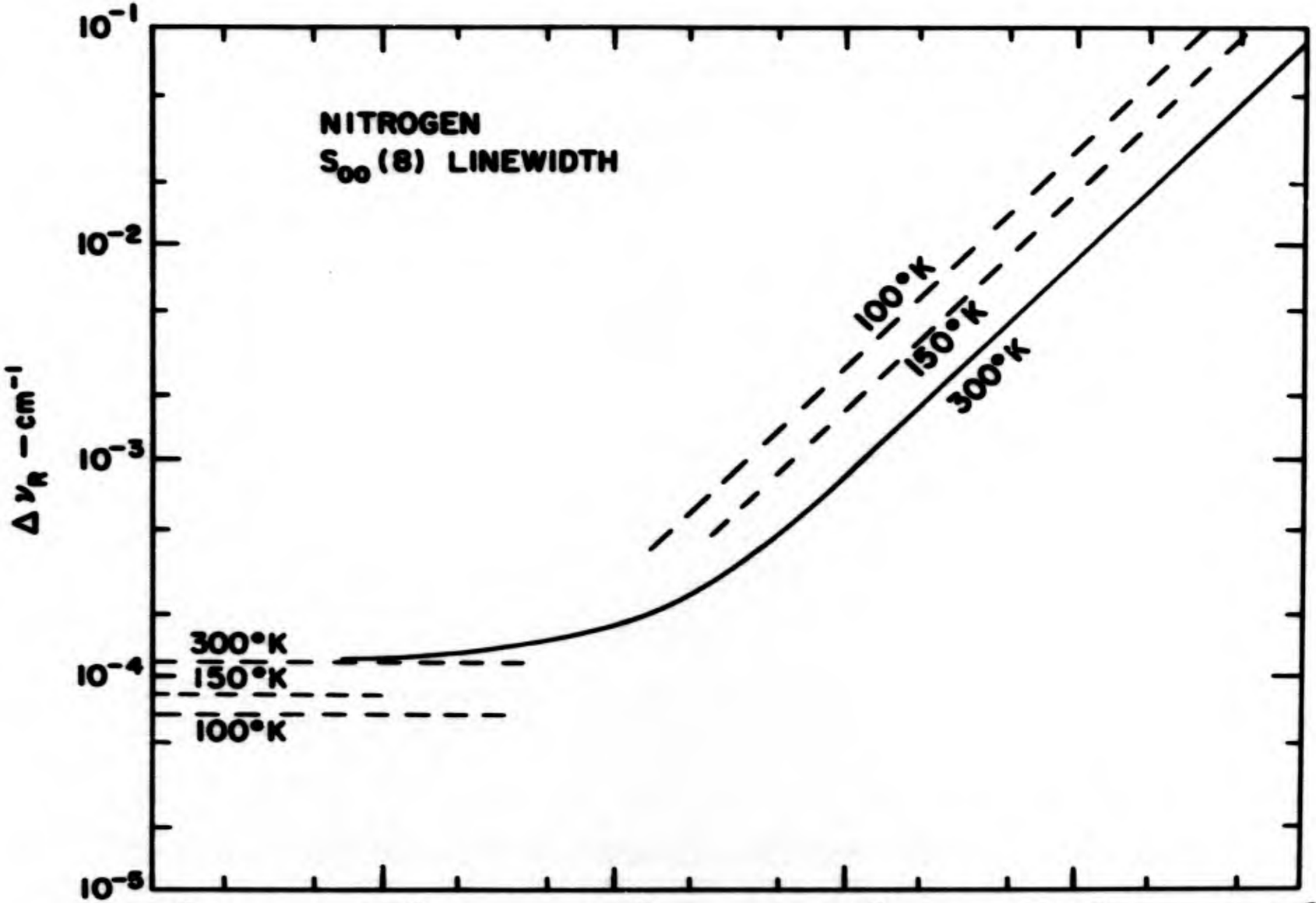
NITROGEN
$S_{00}(8)$ LINEWIDTH
100°K
150°K
300°K
300°K
150°K
100°K
$\Delta\nu_R$ — cm^{-1}
10^{-1}
10^{-2}
10^{-3}
10^{-4}
10^{-5}
10^{-5}
10^{-4}
10^{-3}
10^{-2}
10^{-1}
10^{0}
PRESSURE — ATM.

FIG. 10

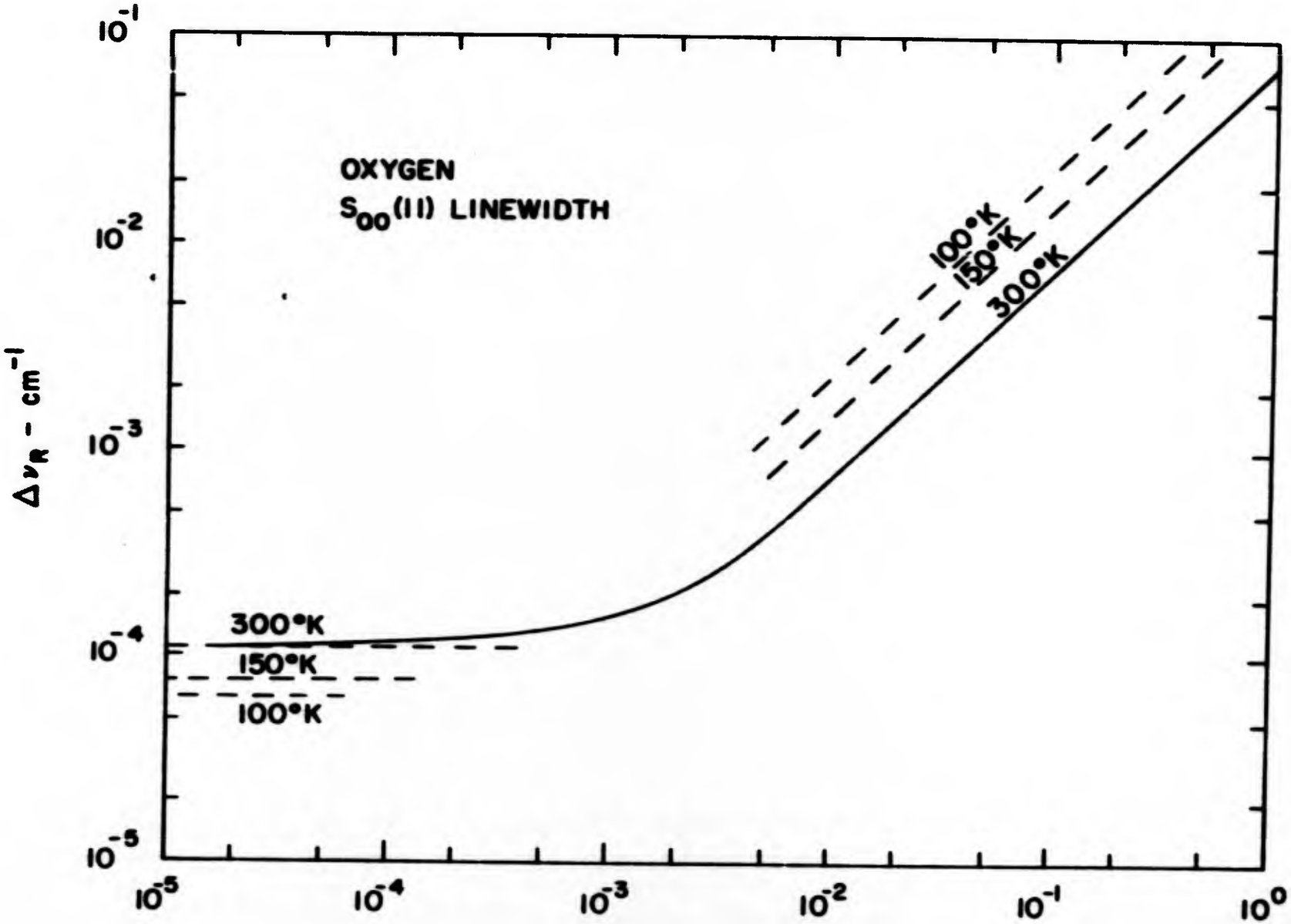
OXYGEN
$S_{00}(11)$ LINEWIDTH
100°K
150°K
300°K
300°K
150°K
100°K
$\Delta\nu_R$ - cm^{-1}
10^{-1}
10^{-2}
10^{-3}
10^{-4}
10^{-5}
10^{-5}
10^{-4}
10^{-3}
10^{-2}
10^{-1}
10^{0}
PRESSURE - ATM

Fig. 11

$(1-A')/\tau_L$ is chosen proportional to the number of collisions (CPT^{-1} rather than CPT^{-x} with $x \approx .9$ as is estimated from certain experiments[18]) having a value at room temperature corresponding to the measured coefficient for the transition and gas of interest. A change of variables reduces (17) to

$$I(0) = \frac{e^b}{\pi\beta} \int_0^1 u^{-(1-a/\beta)} \; e^{-bu} \; du \qquad (19)$$

where $$b = \frac{D}{\beta}\left(\frac{2\pi}{\lambda'}\right)^2$$

$$a = (1 + A')/\tau_L + D\left(\frac{2\pi}{\lambda'}\right)^2$$

Equation (19) can be evaluated by a series expansion, although several special cases can be more directly calculated. For $\beta \to \infty$, $I(0) \to \frac{1}{\pi a}$ which corresponds to the high pressure region and demonstrates both pressure broadening and Dicke's version of motional narrowing. For $\beta \to 0$, the distribution goes to the doppler limit (more easily seen from (17)). The intermediate points were calculated for several values of a/β: (1/16, 1/4, 0.35, 1/2, 1, 2, 4, 16, and 64) for which the integral (19) was numerically evaluated. At fixed temperature the pressure was chosen to give a/β the desired ratio, and the resulting effective linewidth was then plotted for the pressure which corresponds to the a/β value.

5) Normalized Gain Coefficient

The calculations of the normalized power gain coefficient, g, follows in a straightforward manner from Eq. (4) and the previous numerical evaluations. The values for the various transitions as functions of temperature and pressure are shown in Figures 12 to 18. Again, the reader is cautioned that these calculations are subject to the approximations involved

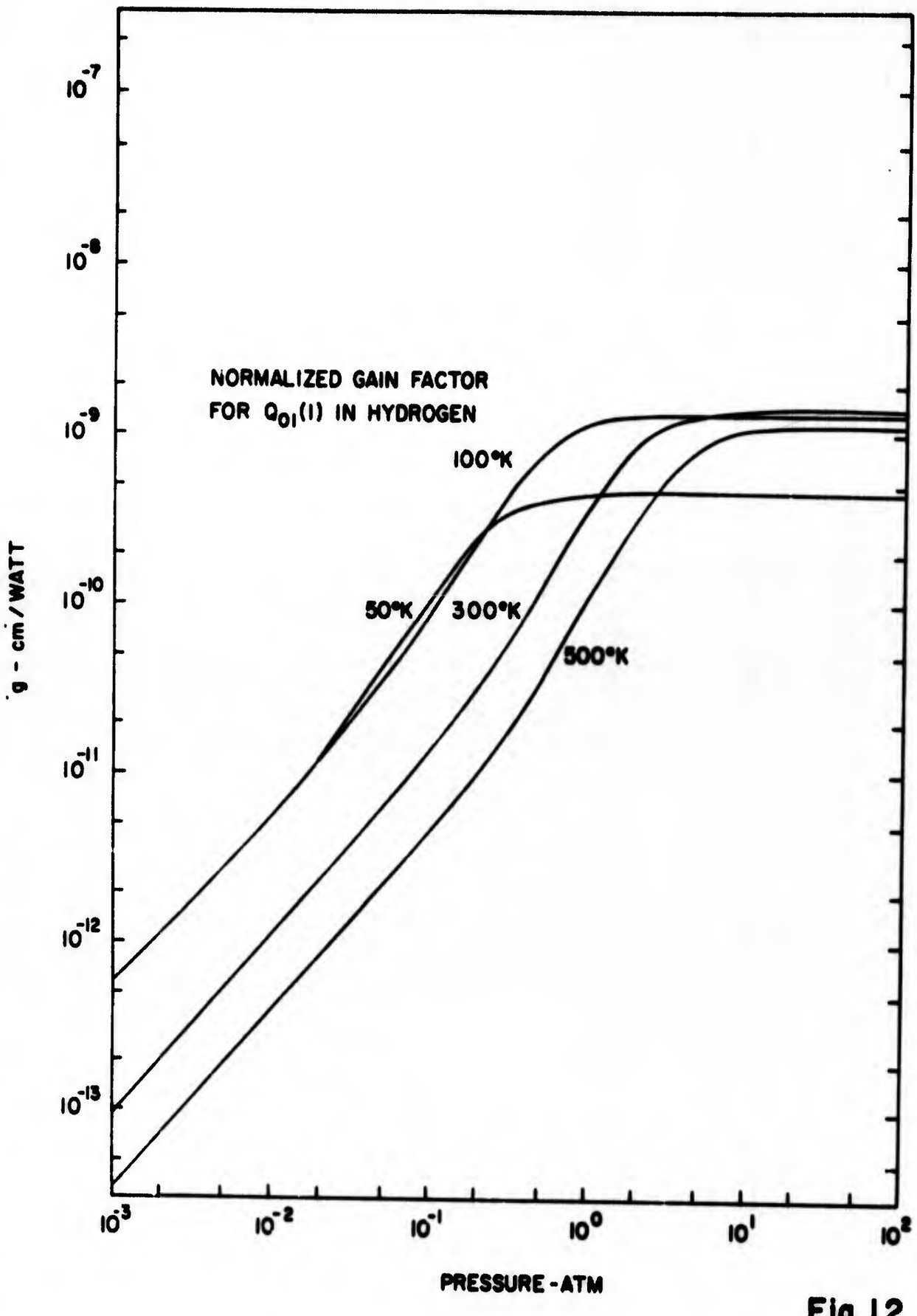
NORMALIZED GAIN FACTOR
FOR $Q_{01}(1)$ IN HYDROGEN
100°K
50°K
300°K
500°K
g - cm / WATT
10^{-7}
10^{-8}
10^{-9}
10^{-10}
10^{-11}
10^{-12}
10^{-13}
10^{-3}
10^{-2}
10^{-1}
10^{0}
10^{1}
10^{2}
PRESSURE - ATM

Fig. 12

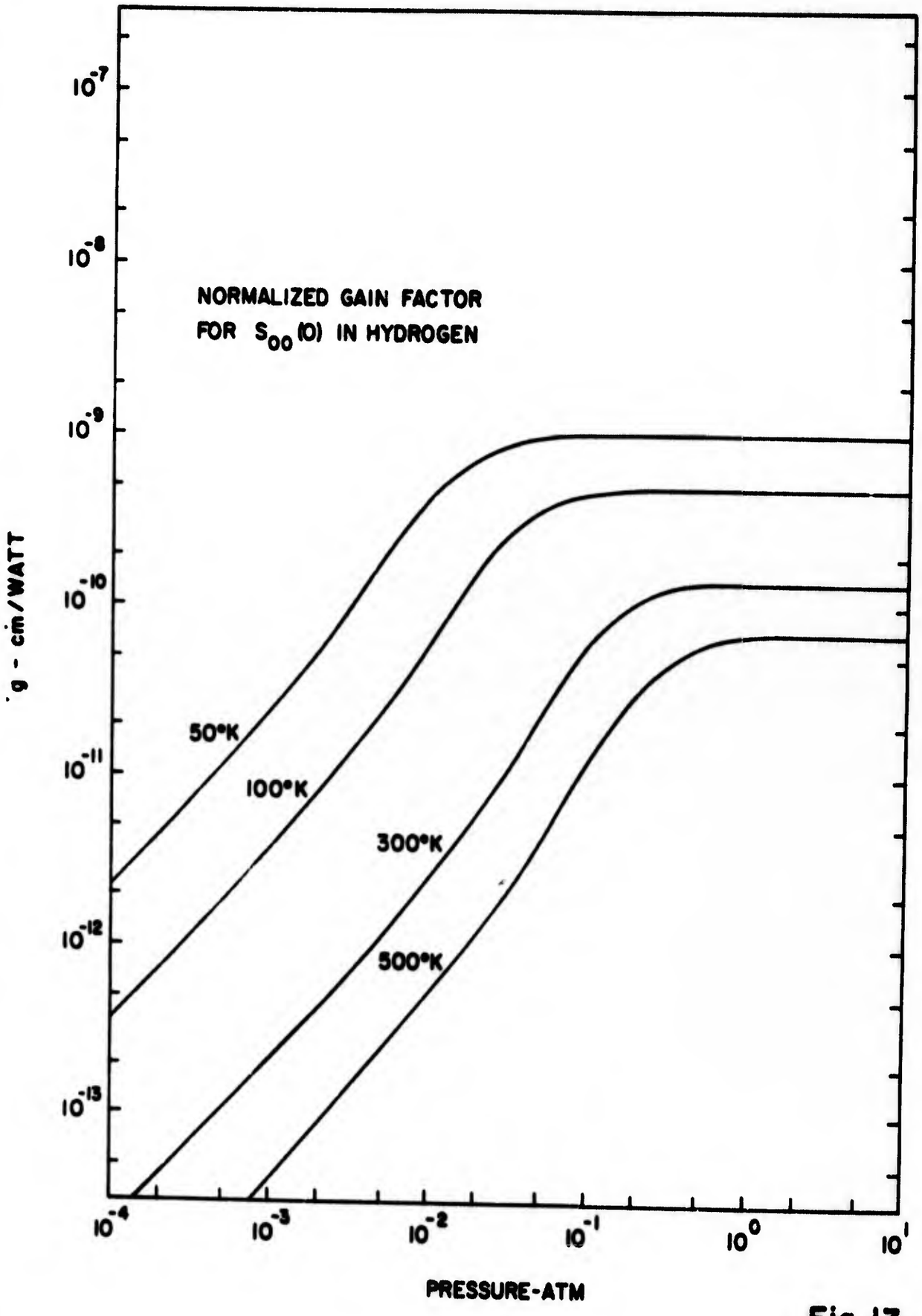
NORMALIZED GAIN FACTOR
FOR $S_{00}(0)$ IN HYDROGEN
10^{-7}
10^{-8}
10^{-9}
10^{-10}
10^{-11}
10^{-12}
10^{-13}
g - cm/WATT
50°K
100°K
300°K
500°K
10^{-4}
10^{-3}
10^{-2}
10^{-1}
10^{0}
10^{1}
PRESSURE-ATM

Fig. 13

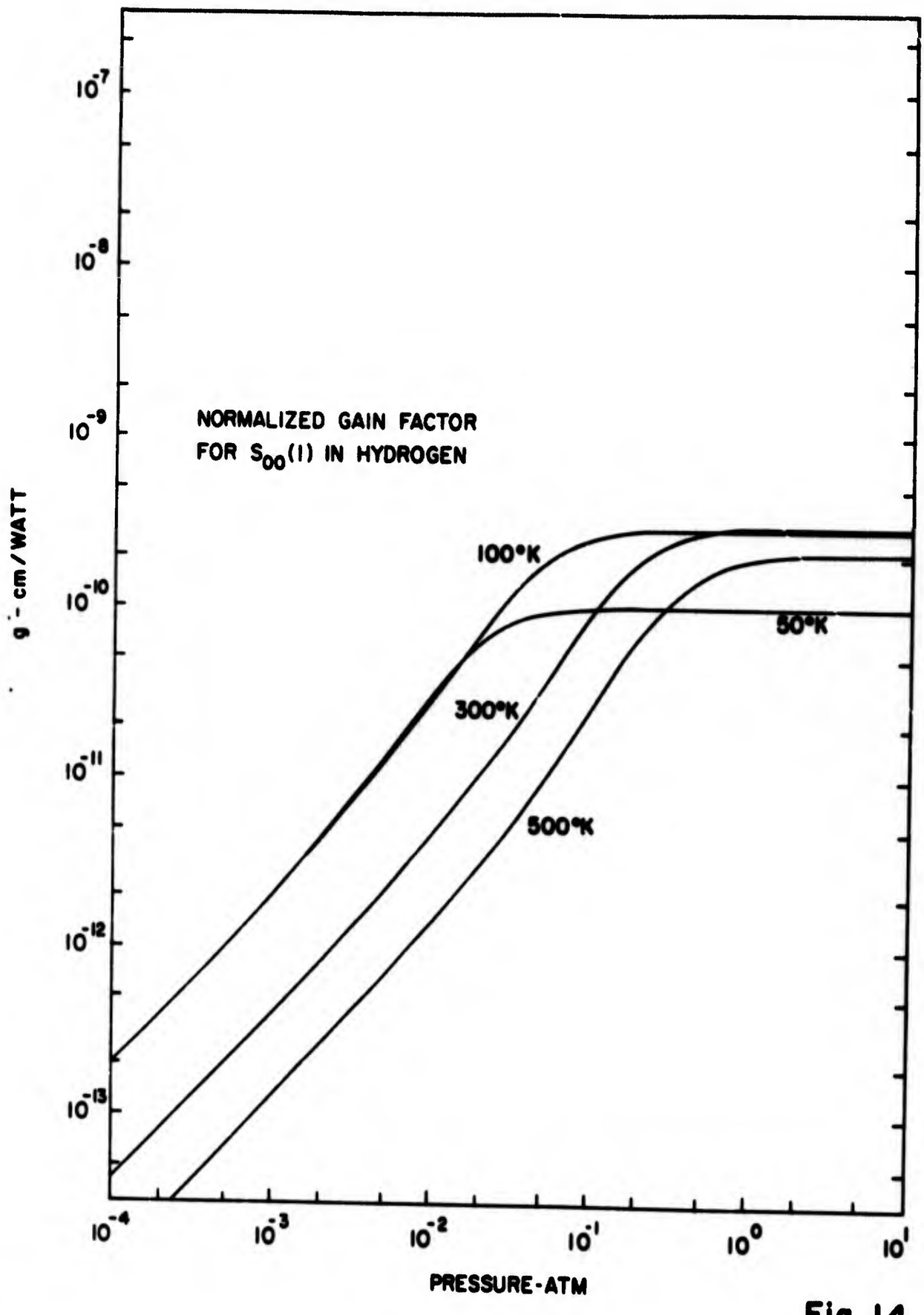
NORMALIZED GAIN FACTOR
FOR $S_{00}(1)$ IN HYDROGEN
100°K
50°K
300°K
500°K
g - cm / WATT
10^{-7}
10^{-8}
10^{-9}
10^{-10}
10^{-11}
10^{-12}
10^{-13}
10^{-4}
10^{-3}
10^{-2}
10^{-1}
10^{0}
10^{1}
PRESSURE-ATM

Fig. 14

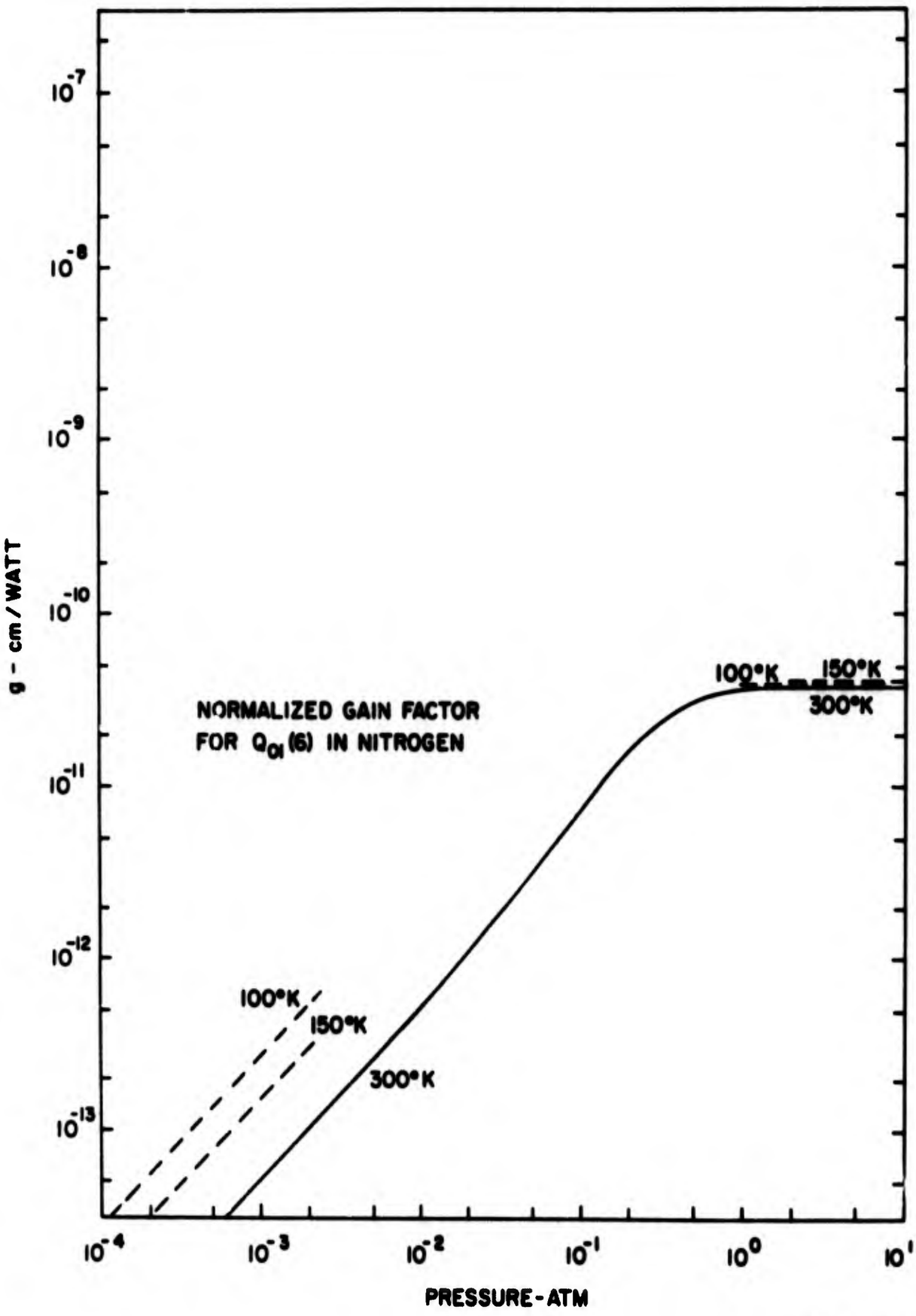
10^{-7}
10^{-8}
10^{-9}
10^{-10}
10^{-11}
10^{-12}
10^{-13}
g - cm / WATT
NORMALIZED GAIN FACTOR
FOR $Q_{01}(6)$ IN NITROGEN
100°K
150°K
300°K
100°K
150°K
300°K
10^{-4}
10^{-3}
10^{-2}
10^{-1}
10^{0}
10^{1}
PRESSURE - ATM

Fig. 15

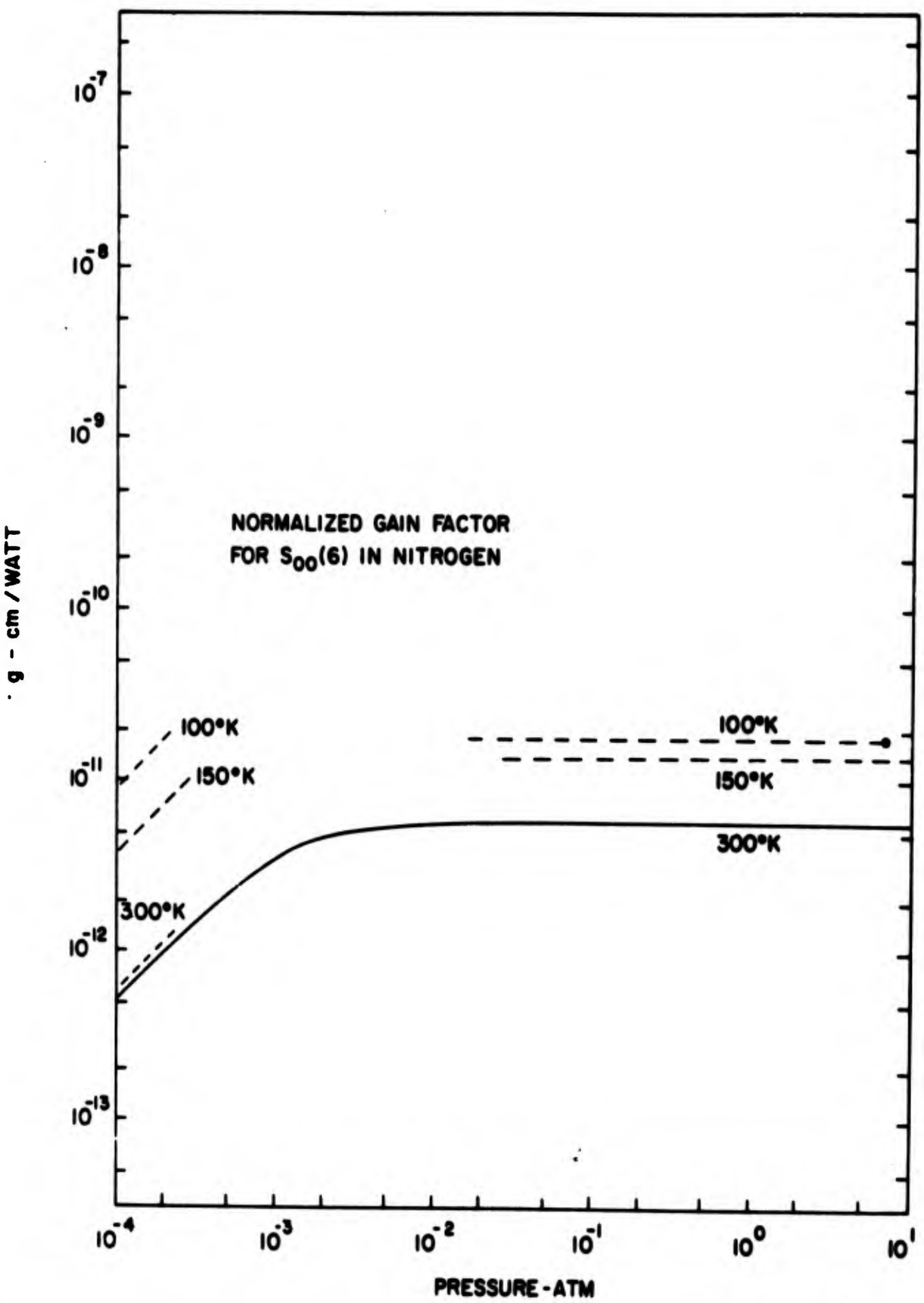
NORMALIZED GAIN FACTOR
FOR $S_{00}(6)$ IN NITROGEN
100°K
150°K
300°K
100°K
150°K
300°K
10^{-7}
10^{-8}
10^{-9}
10^{-10}
10^{-11}
10^{-12}
10^{-13}
10^{-4}
10^{-3}
10^{-2}
10^{-1}
10^{0}
10^{1}
g - cm / WATT
PRESSURE - ATM

Fig. 16

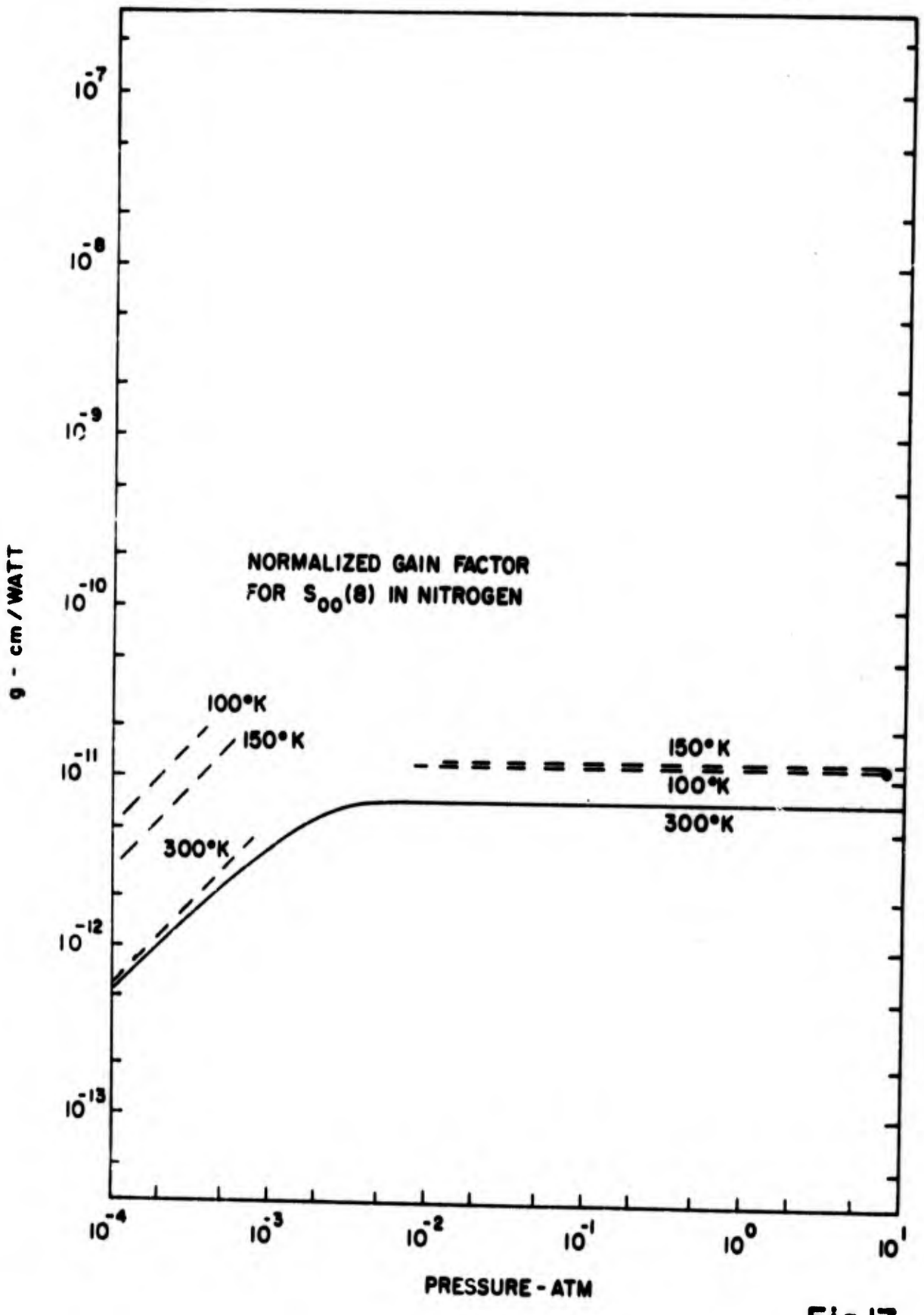
NORMALIZED GAIN FACTOR
FOR $S_{00}(8)$ IN NITROGEN
g - cm / WATT
PRESSURE - ATM
100°K
150°K
300°K
150°K
100°K
300°K
10^{-7}
10^{-8}
10^{-9}
10^{-10}
10^{-11}
10^{-12}
10^{-13}
10^{-4}
10^{-3}
10^{-2}
10^{-1}
10^{0}
10^{1}

Fig 17

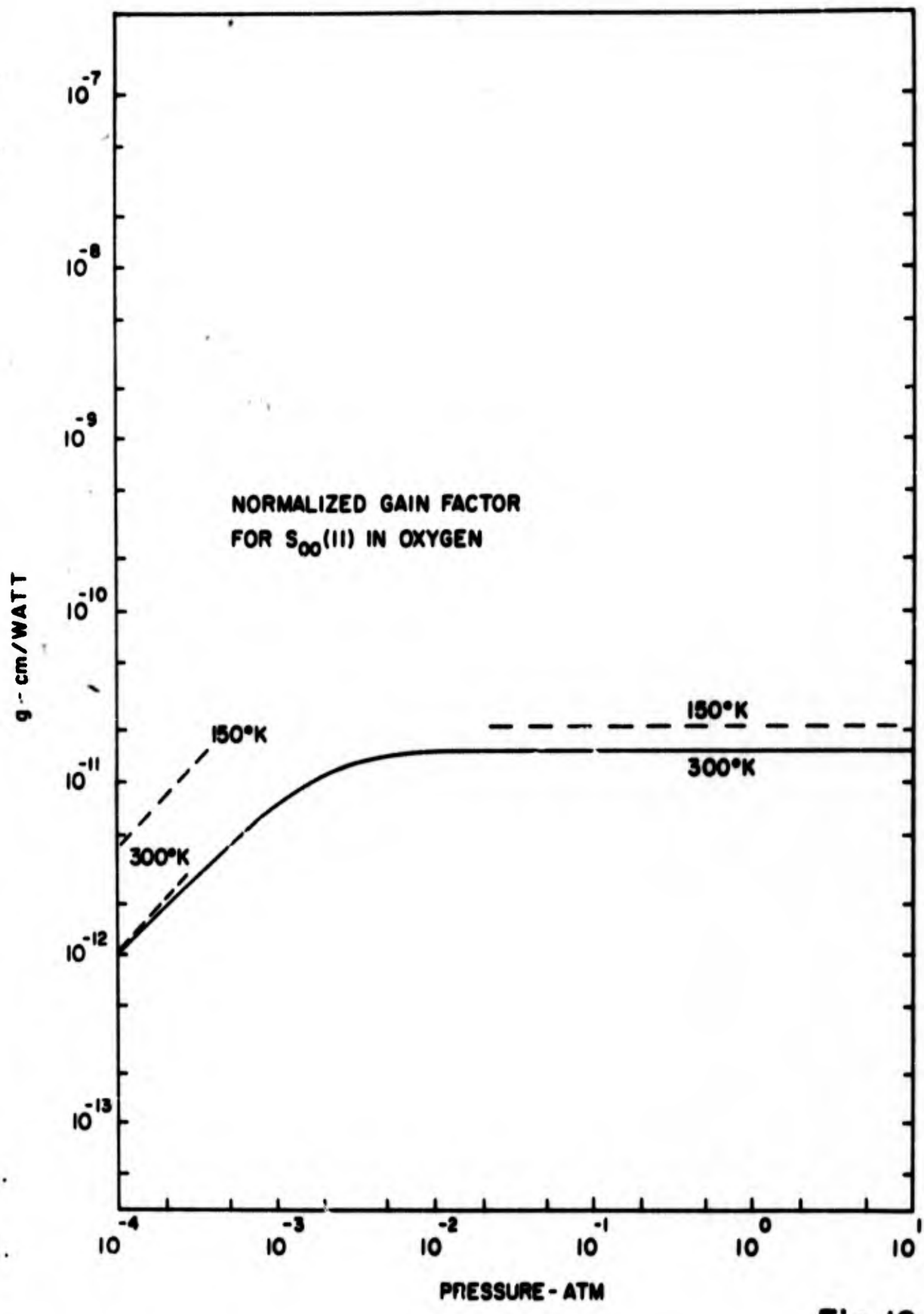
NORMALIZED GAIN FACTOR
FOR $S_{00}(11)$ IN OXYGEN
g - cm/WATT
10^{-7}
10^{-8}
10^{-9}
10^{-10}
10^{-11}
10^{-12}
10^{-13}
150°K
300°K
150°K
300°K
10^{-4}
10^{-3}
10^{-2}
10^{-1}
10^{0}
10^{1}
PRESSURE - ATM

Fig. 18

in the simplified model. One of these is that the laser linewidth is narrow compared to that of the transition, many of which are less than 10^{-3} cm^{-1}.

Experimental comparison will be made in section IV.

III

B. Brillouin

The numerical calculations for brillouin gain are less easily tabulated because the effects of the deviations from the ideal gas law behavior are appreciable and cannot be neglected. Since the actual values of density,[19] compressibility, and viscosity must be used, it is necessary to evaluate the gain from Eq. (10) for each value of temperature and pressure.

Once again, in order to estimate the importance of transient behavior, it is convenient to know the acoustic losses, hence the linewidth, as a function of the gas parameters. For low losses (where the normal mode formulism holds) the linewidth (full width at half height) can be shown to be

$$\Delta\nu_B = \beta k_B^2/\pi\rho \qquad (20)$$

$$\text{where } \beta = \eta v + (\gamma-1)\frac{K}{c_p}$$

$$= \eta\left[v + \frac{\gamma-1}{P_r}\right]$$

where η is the viscosity, v is the viscosity number having a value of about 4/3, γ is the ratio of specific heats, and P_r is the Prandtl number.

At low gas pressures, the losses can become so high that the linewidth exceeds the frequency shift. However, the original model of a continuous

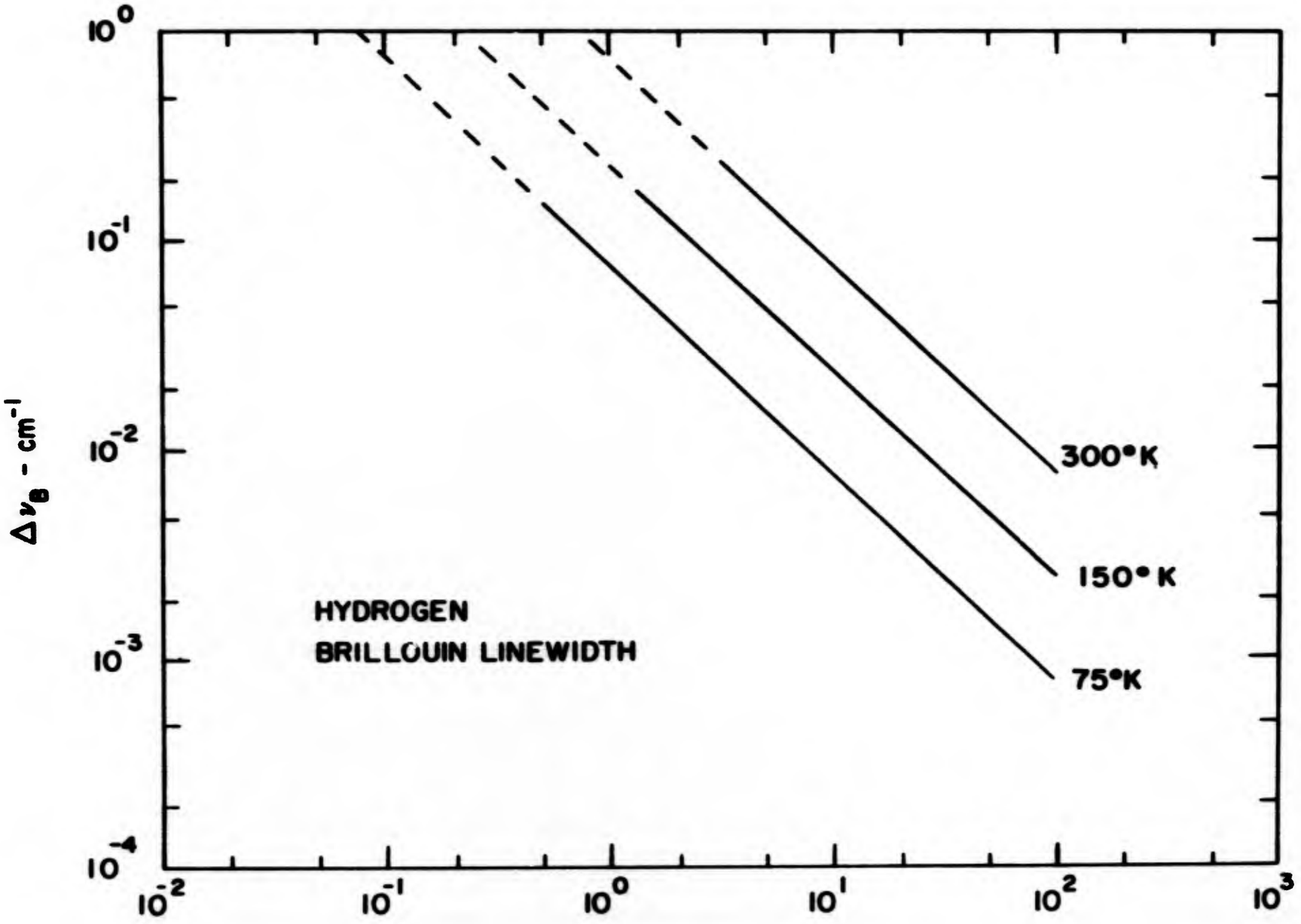
10^0
10^{-1}
10^{-2}
10^{-3}
10^{-4}
$\Delta\nu_B$ - cm^{-1}
300°K
150°K
75°K
HYDROGEN
BRILLOUIN LINEWIDTH
10^{-2}
10^{-1}
10^0
10^1
10^2
10^3
PRESSURE - ATM

Fig. 19

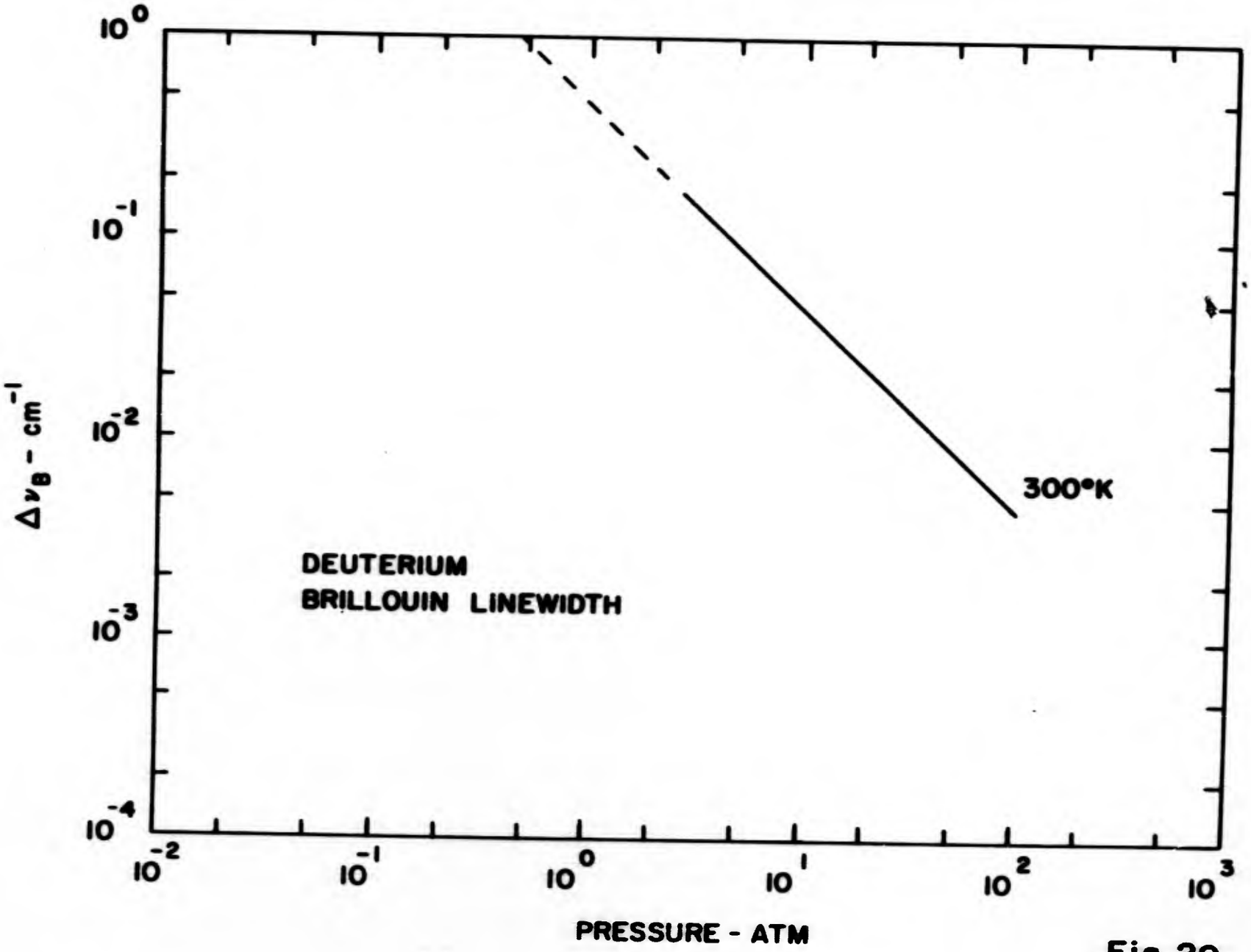
10^0
10^{-1}
10^{-2}
10^{-3}
10^{-4}
$\Delta\nu_B$ - cm^{-1}
300°K
DEUTERIUM
BRILLOUIN LINEWIDTH
10^{-2}
10^{-1}
10^0
10^1
10^2
10^3
PRESSURE - ATM

Fig. 20

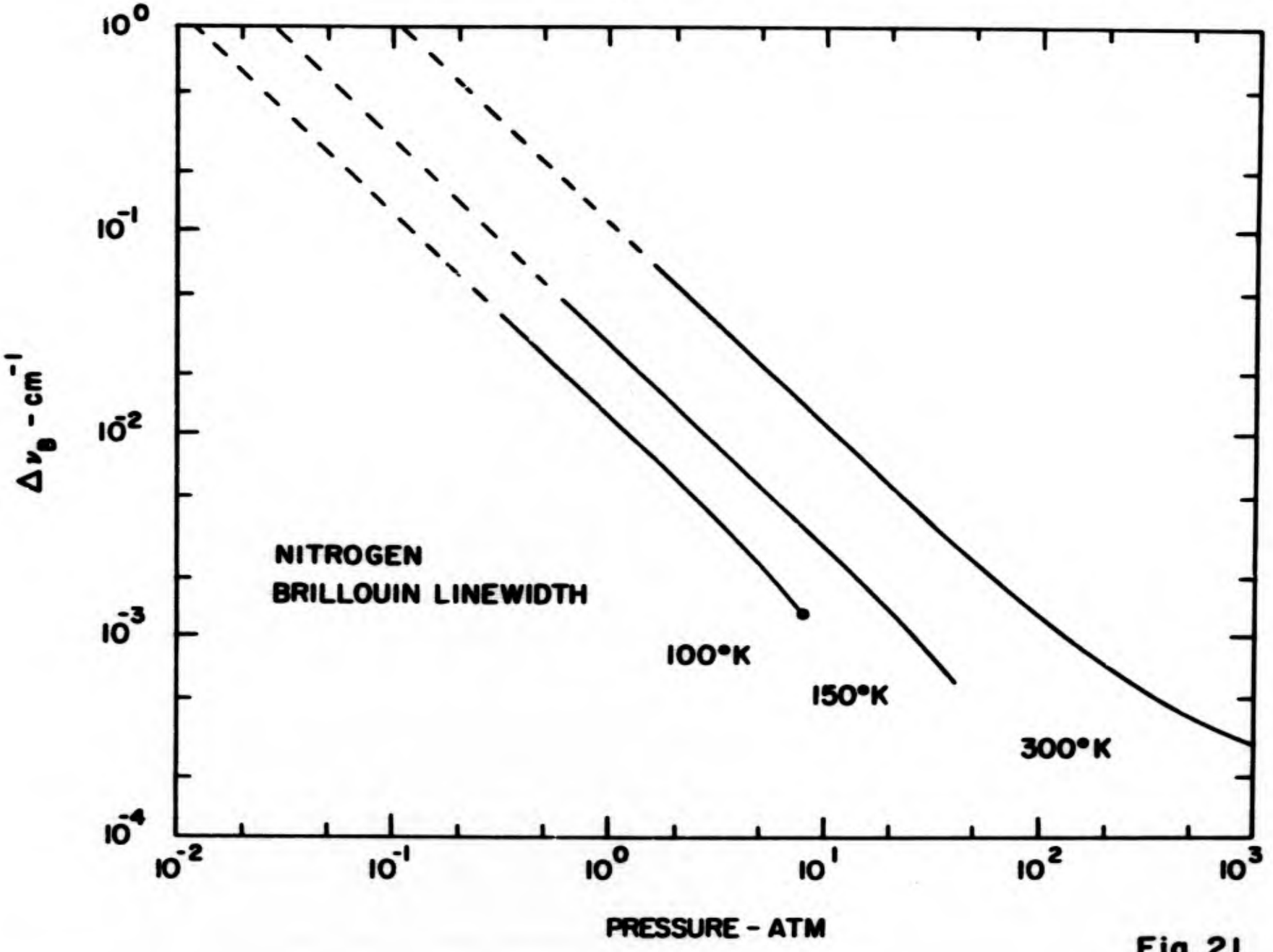
10^0
10^{-1}
10^{-2}
10^{-3}
10^{-4}
$\Delta\nu_B$ - cm^{-1}
NITROGEN
BRILLOUIN LINEWIDTH
100°K
150°K
300°K
10^{-2}
10^{-1}
10^0
10^1
10^2
10^3
PRESSURE - ATM

Fig. 21

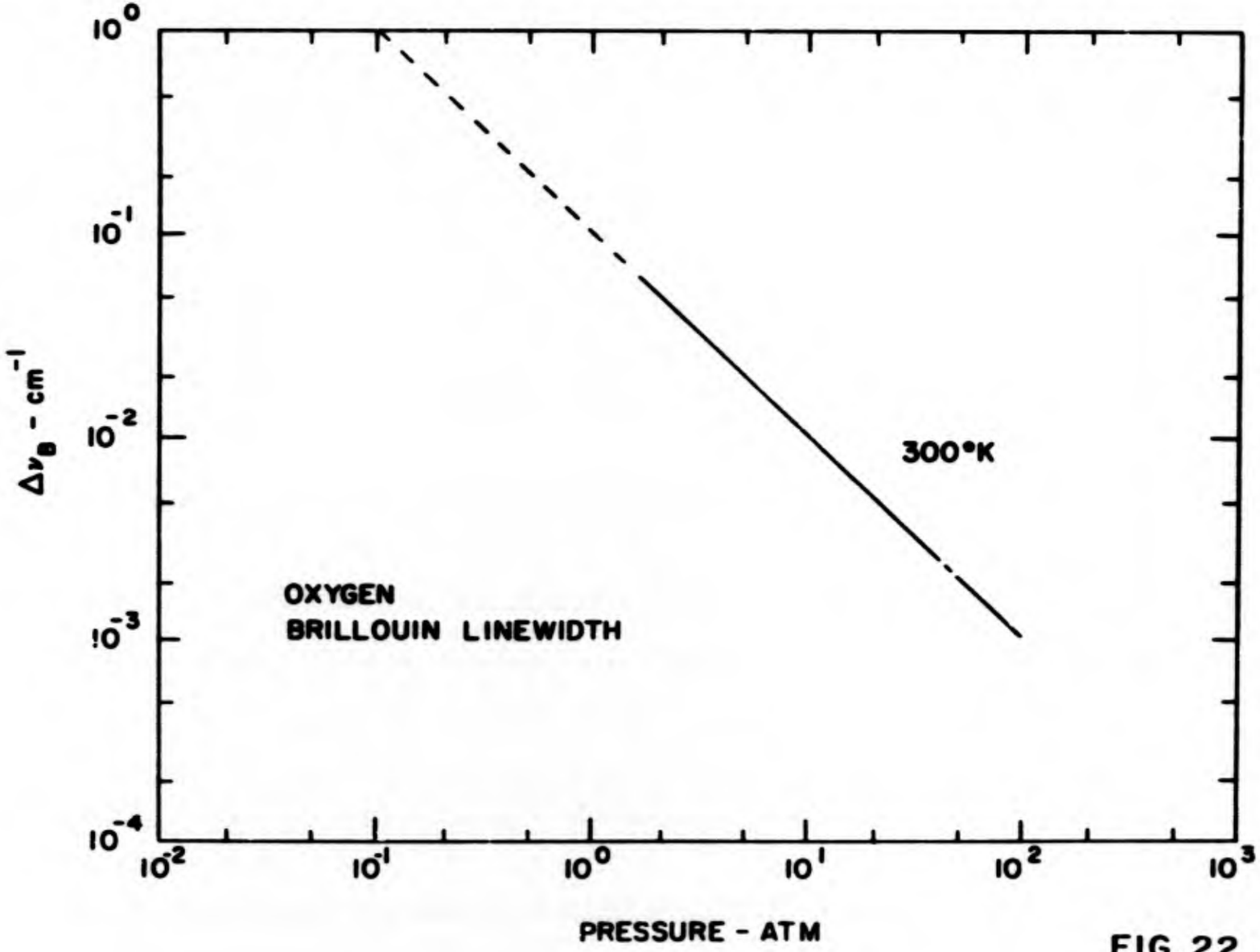
10^0
10^{-1}
10^{-2}
10^{-3}
10^{-4}
$\Delta\nu_B$ - cm^{-1}
300°K
OXYGEN
BRILLOUIN LINEWIDTH
10^{-2}
10^{-1}
10^0
10^1
10^2
10^3
PRESSURE - ATM

FIG. 22

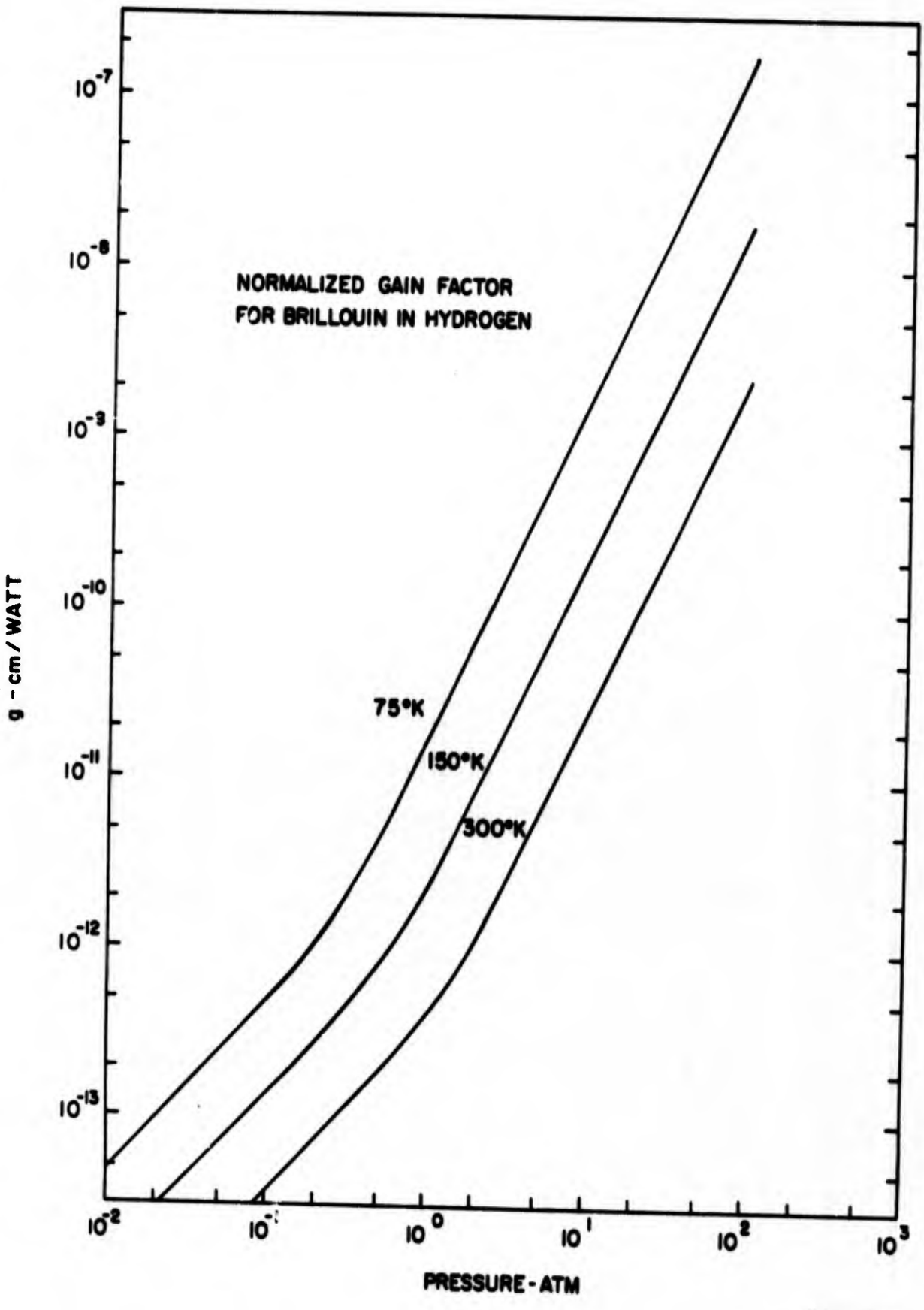
NORMALIZED GAIN FACTOR
FOR BRILLOUIN IN HYDROGEN
75°K
150°K
300°K
g - cm / WATT
PRESSURE - ATM
10^-7
10^-8
10^-9
10^-10
10^-11
10^-12
10^-13
10^-2
10^-1
10^0
10^1
10^2
10^3

Fig.23

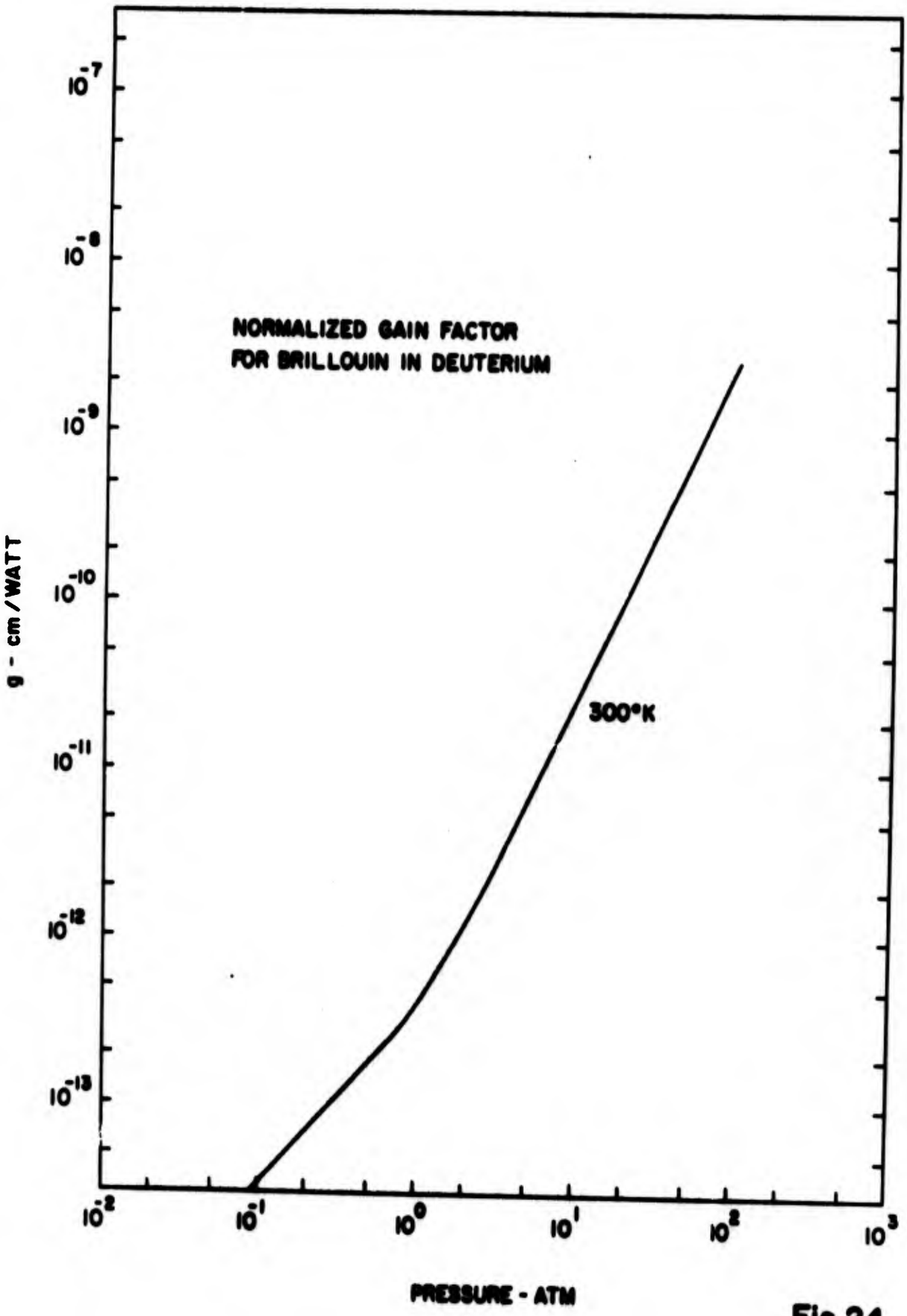
NORMALIZED GAIN FACTOR
FOR BRILLOUIN IN DEUTERIUM
300°K
g - cm / WATT
PRESSURE - ATM
10^-7
10^-8
10^-9
10^-10
10^-11
10^-12
10^-13
10^-2
10^-1
10^0
10^1
10^2
10^3

Fig.24

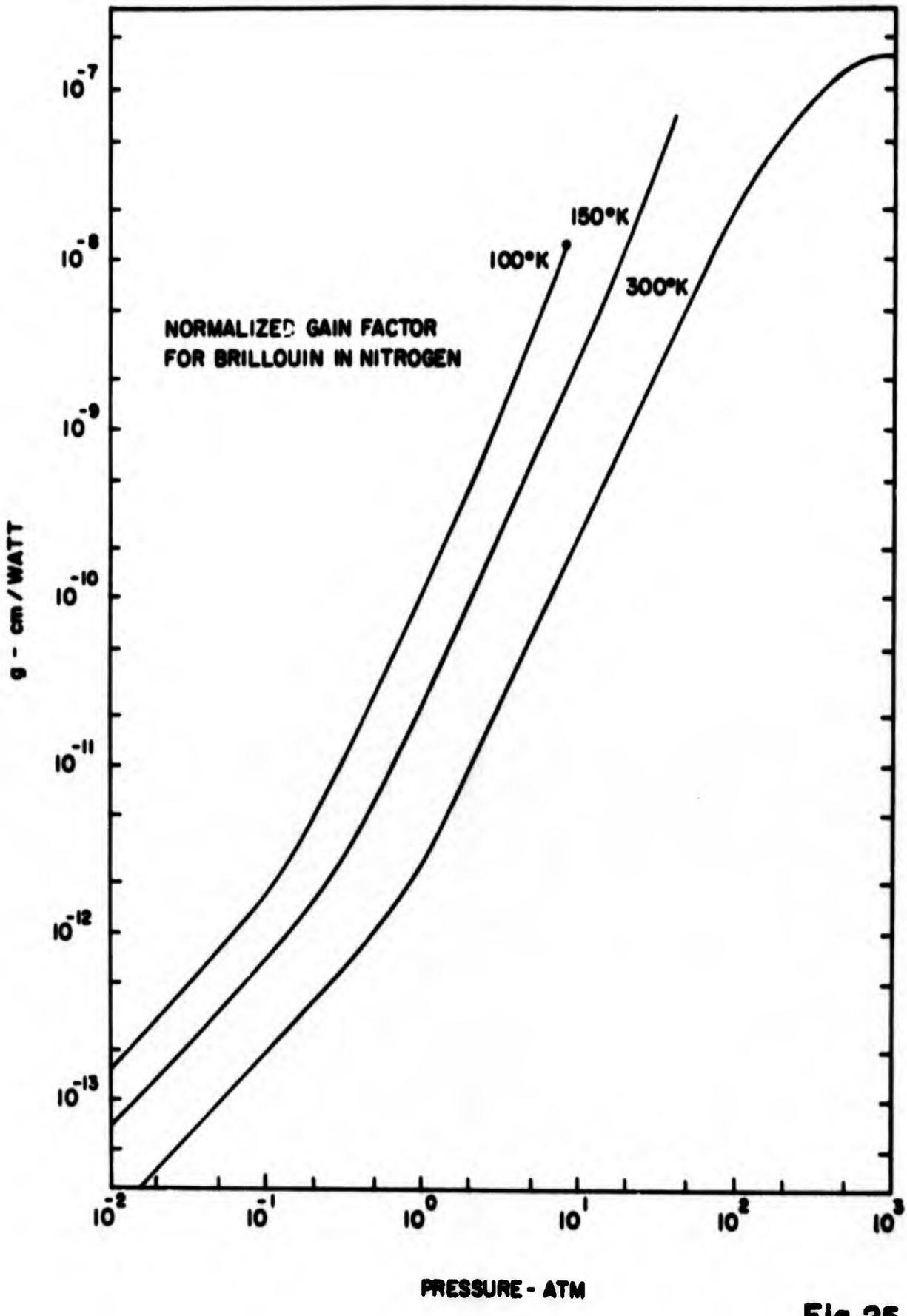
NORMALIZED GAIN FACTOR
FOR BRILLOUIN IN NITROGEN
100°K
150°K
300°K
g - cm / WATT
PRESSURE - ATM

Fig. 25

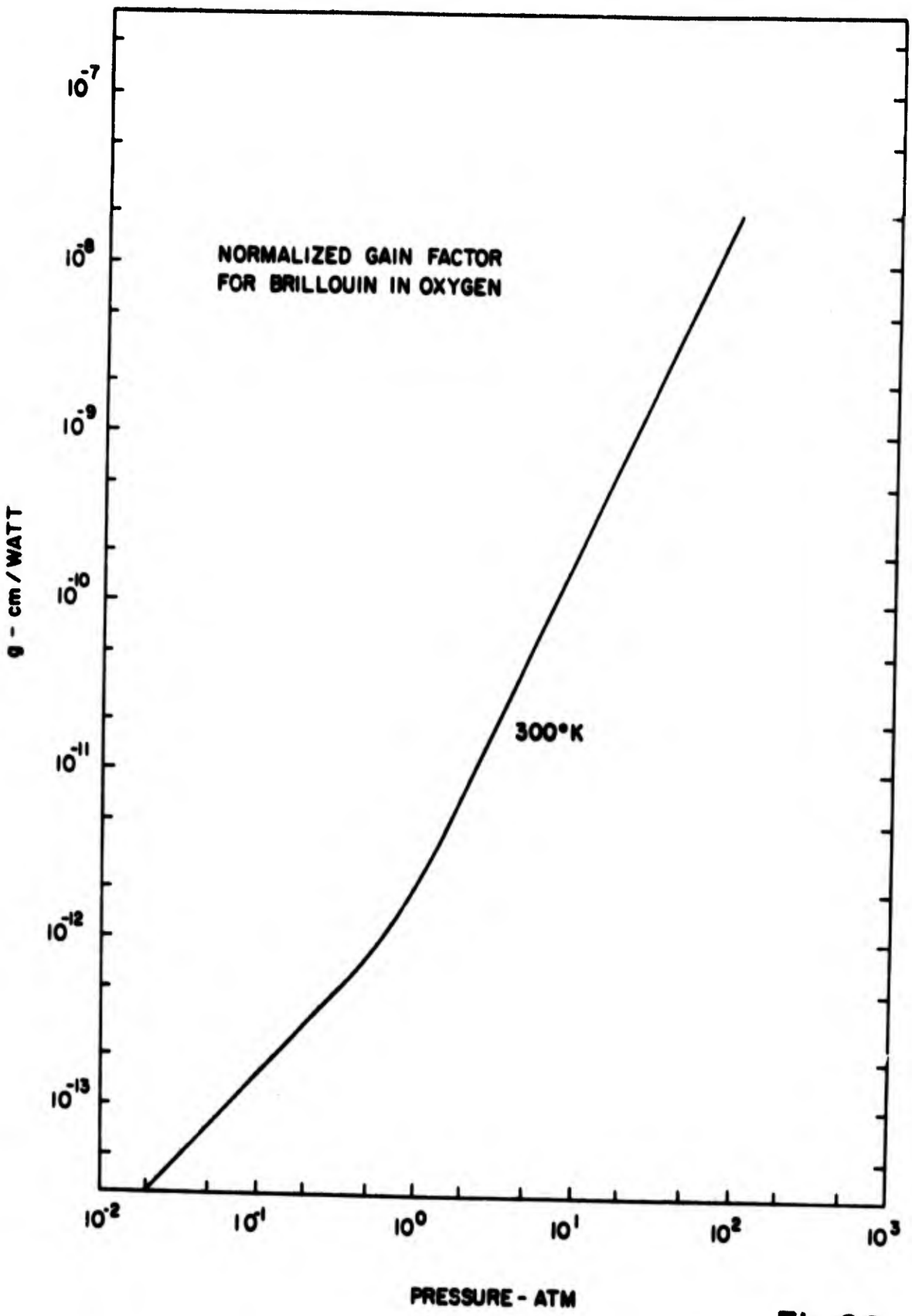
NORMALIZED GAIN FACTOR
FOR BRILLOUIN IN OXYGEN
300°K
g - cm / WATT
10^{-7}
10^{-8}
10^{-9}
10^{-10}
10^{-11}
10^{-12}
10^{-13}
10^{-2}
10^{-1}
10^{0}
10^{1}
10^{2}
10^{3}
PRESSURE - ATM

Fig.26

total gain is estimated to be about exp (30) by using the most intense region of the focused beam (an imaginary flux tube on the axis), one would then expect the contributions from other regions to be negligible if they correspond to laser intensities of less than 90 to 95% of the intensity on axis at that cross section. The stokes beam would then experience high gain only in the central region near the axis.

Neglecting possible trapping effects due to dispersion in the high gain region, the diffraction losses of a beam that size would negate most of the gain that would have been expected. Continuing the numerology, a model consistent with high gain and moderate diffraction loss occurs for the 80 to 85% power contour of the focused beam. Based on the 85% curve, the computed ratio for ℓ/A is $5n/\lambda$. For real laser beams, one expects non-diffraction limited behavior and a lower ℓ/A ratio. Assuming that to be observable, the Stokes wave must have a minimum integrated gain of exp (30), a value for the product $g\,\ell/A$ can then be computed from a measurement of threshold laser power -- $g\,\ell/A = \frac{30}{P_L}$. One could then hope that the effective length to area ratio would be repeatable during an experiment so that a variation of threshold power would imply the inverse change in g as some parameter is changed. The inverse of threshold laser powers are plotted in Figures 27 and 28 with an adjustable scale factor to allow the best fit with the calculated gain curves. To account for the transient conditions which prevail for many of the experimental situations, a detailed analysis similar to that of Kroll[2] must be employed. One can obtain a transient gain curve for sbs by use of Kroll's approximate equations. The amount by which the gain is reduced is dependent on laser power, so that it is not simply possible to form a derating factor based on linewidths of the transition

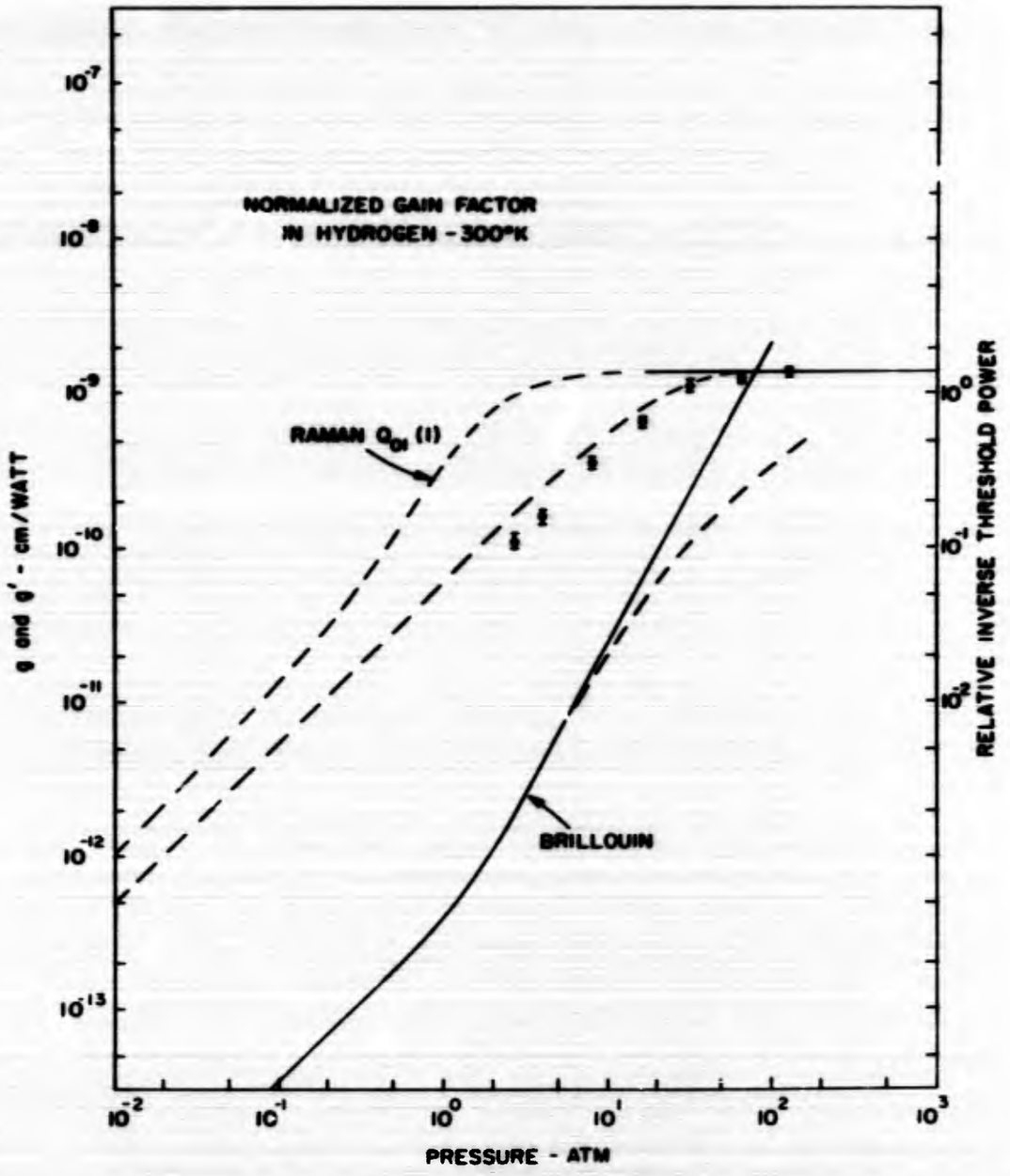
NORMALIZED GAIN FACTOR
IN HYDROGEN - 300°K
RAMAN Q_{01} (1)
BRILLOUIN
g and g' - cm/WATT
RELATIVE INVERSE THRESHOLD POWER
PRESSURE - ATM
10^{-7}
10^{-8}
10^{-9}
10^{-10}
10^{-11}
10^{-12}
10^{-13}
10^{0}
10^{-1}
10^{-2}
10^{-2}
10^{-1}
10^{0}
10^{1}
10^{2}
10^{3}

Fig.27

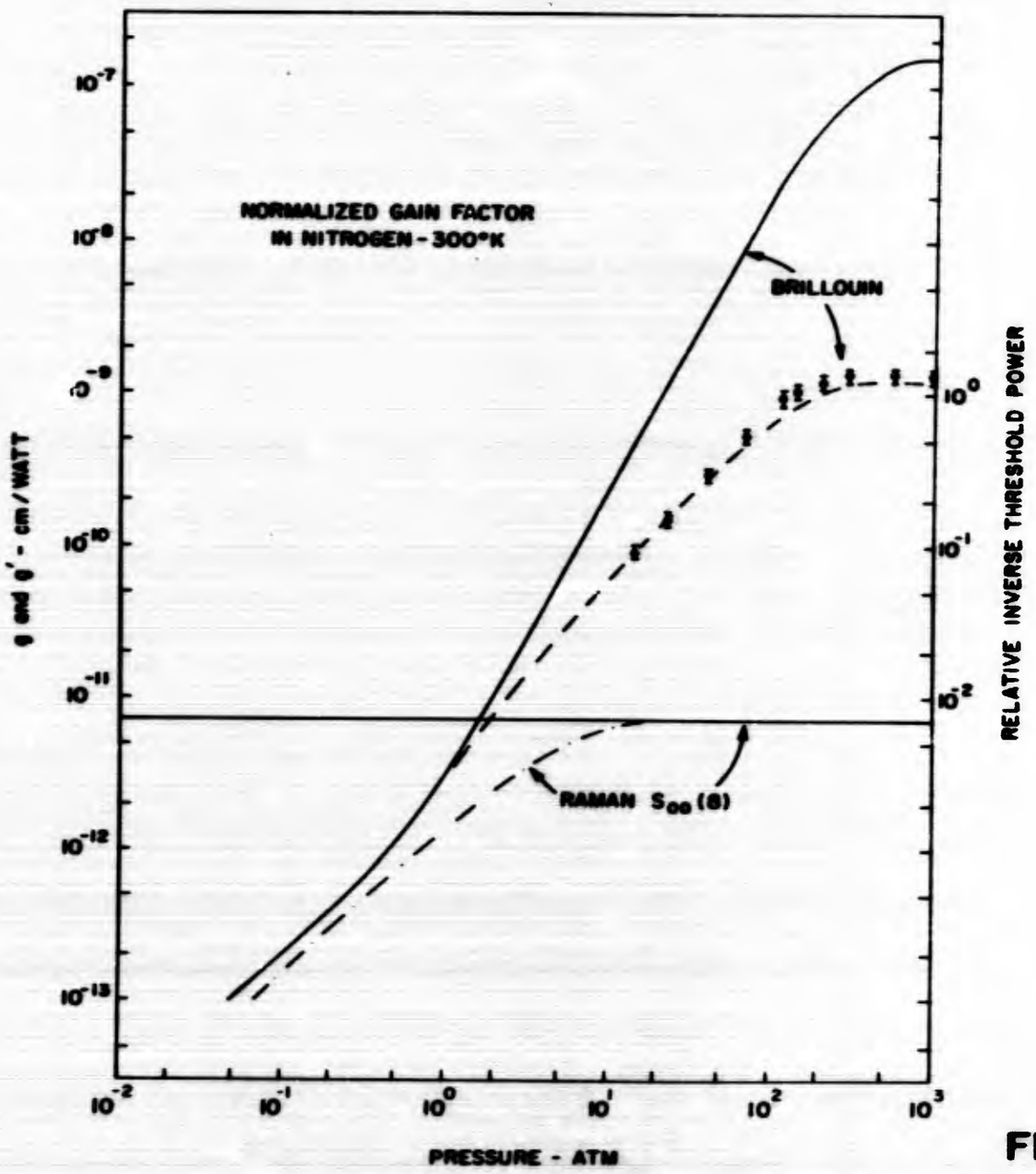
NORMALIZED GAIN FACTOR
IN NITROGEN - 300°K
BRILLOUIN
RAMAN $S_{00}(\delta)$
g and g' - cm / WATT
RELATIVE INVERSE THRESHOLD POWER
PRESSURE - ATM
10^{-7}
10^{-9}
10^{-11}
10^{-13}
10^{0}
10^{-1}
10^{-2}
10^{-2}
10^{-1}
10^{0}
10^{1}
10^{2}
10^{3}

FIG. 28

and the laser. However the ratio of transient to steady state gain at fixed gas pressure which is given by

$$R = \frac{g'}{g} = \frac{2[\sqrt{2}\,(xvt + v^2t^2)^{\frac{1}{2}}\,(g\,I_\ell\,\alpha)^{\frac{1}{2}} - \alpha vt]}{g\,I_\ell\,x} \qquad (21)$$

where g is the normalized power gain for a monochromatic laser

I_ℓ is the laser intensity

and other symbols are given by Kroll.

can be evaluated by requiring that the transient gain must be some large fixed value (say exp (30)). Requiring that the numerator be equal to 30, the ratio becomes

$$R = \frac{60\alpha\,(xvt + v^2t^2)}{x\,(15 + \alpha vt)^2} = \frac{4 \cdot \frac{30}{\pi\Delta\nu t}}{\left(1 + \frac{30}{\pi\Delta\nu t}\right)^2} \qquad t < \frac{30}{\pi\Delta\nu} \qquad (22)$$

Although t is intended by Kroll to represent the pulse duration, many factors can shorten it and make it uncertain. Treating t as a parameter, a value can be chosen which optimizes the fit. For reasons to be discussed later, a time of 2 nsec is used for all data presented here. The scale factors used in Fig. 27 and 28 to adjust the inverse threshold power to fit the transient gain curves are 3 and 2.5 assuming $g' = \frac{30}{P_L\,\ell/A}$ and $\ell/A = 5\pi/\lambda$ as previously discussed. Considering the uncertainties in spatial properties and frequency characteristics of the laser, the agreement is excellent, both in relative and in absolute values.

Since both srs and sbs exhibit exponential growth and have the same dependence on the laser power, the processes will compete. However, the variation of gain with pressure at fixed temperature is different for

the two processes as seen in Figures 27 and 28. The calculated threshold for sbs is very dependent on temperature, varying about as T^{-3}, due to increased particle density and to smaller acoustic losses. It should therefore be possible to select which process is stimulated by choosing the proper temperature and pressure, providing sufficient laser power is available. The calculated gain curves for H_2 at 77°K are given in Fig. 29 showing that the crossover between srs and sbs now falls at an achievable value of gain and pressure.

Experimental results are plotted in Fig. 29, showing that the crossover from srs to sbs is observed as pressure is increased. Near the crossover region, both processes appear simultaneously (observed with fast diodes) and exhibit threshold behavior. The transient gain curves are calculated based on 2 nsec as before. The data for both srs and sbs are adjusted by a single scale factor to fit the srs data at the highest pressure for which srs was still dominant. In this case the scale factor was 1.3, showing not only relative fit, but excellent absolute agreement, even in the high pressure region where sbs was dominant. In this high pressure region, sbs threshold data fit well, but was strongly suppressed at pressures below the crossover.

The cause for this suppression remains uncertain, although many factors have been considered. Depletion of laser power did not suppress sbs in CH_4 (at 300°K) below its crossover. Likewise, sbs in N_2 (at 300°K) failed to show any similar indications of suppression at a pressure corresponding to a brillouin linewidth equal to that for H_2 (77°K) at the crossover. (This linewidth happened to be comparable to a mode separation in

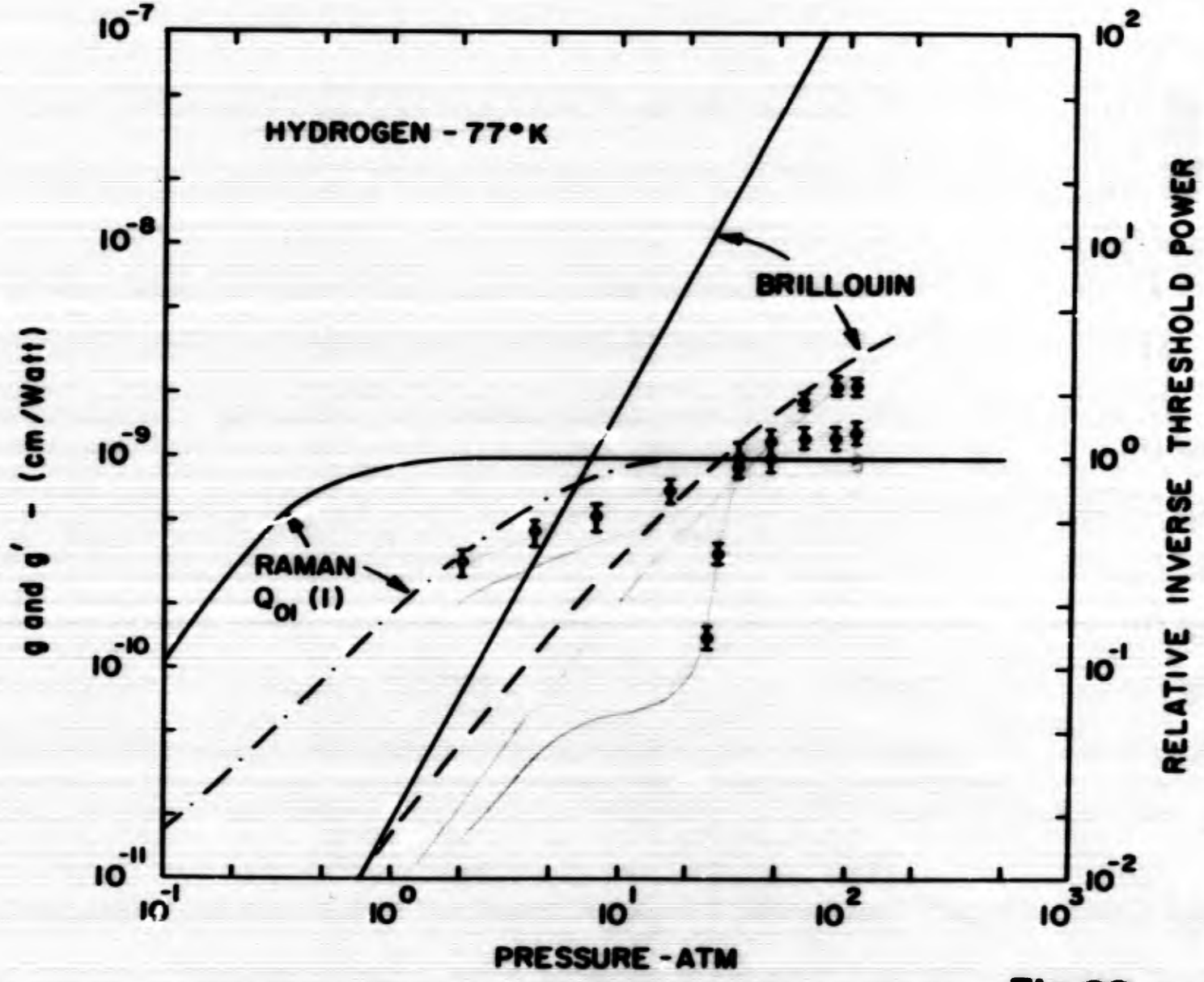
HYDROGEN - 77°K
BRILLOUIN
RAMAN
Q_{01} (1)
g and g' - (cm/Watt)
RELATIVE INVERSE THRESHOLD POWER
PRESSURE - ATM
10^{-7}
10^{-8}
10^{-9}
10^{-10}
10^{-11}
10^{2}
10^{1}
10^{0}
10^{-1}
10^{-2}
10^{-1}
10^{0}
10^{1}
10^{2}
10^{3}

Fig.29

the laser.) The search for other raman lines ($Q_{01}(0)$ and $S_{00}(0)$) which may have absorbed additional laser power, failed to show their existence. Reverse raman has been seen under transient conditions, but is not likely to cause suppression. The effects of these competitions and suppressions will be discussed and reported in detail in a letter to be published elsewhere.[4]

With the correction for transient conditions, the data gave good absolute agreement. However, compared to steady state gain, the experimental value never exceeded it and were as much as two orders of magnitude less. These results imply that anomalous gain did not occur during these focused experiments. This is not unexpected since the critical laser power required for beam trapping in these gases is very large. An attempt to trap in gases gave negative results. Furthermore, to produce a noticeable effect in a focused experiment, the trapping would have to be quite severe.

One of the most interesting observations to come from the data is shown in Fig. 30. On this figure are plotted nearly all the data taken during the past 9 months involving both srs and sbs in several materials, at various temperatures, excited by modified laser systems, and in both focused and parallel beams. The ratio of steady state gain to the experimentally determined values (based on $\ell/A = 5n/\lambda$ for a focus) is plotted versus the linewidth of the transition and found to fit a curve that can be generated by a transient analysis. The time implied by the break in Fig. 30 is 2 nsec. A physical interpretation of this time has not been established. Although much of the data was taken with a laser having a periodic 4 nsec fluctuation, and a gas cell having a 2 nsec double pass length, variations from these experimental conditions gave data in the same agreement with the curve.

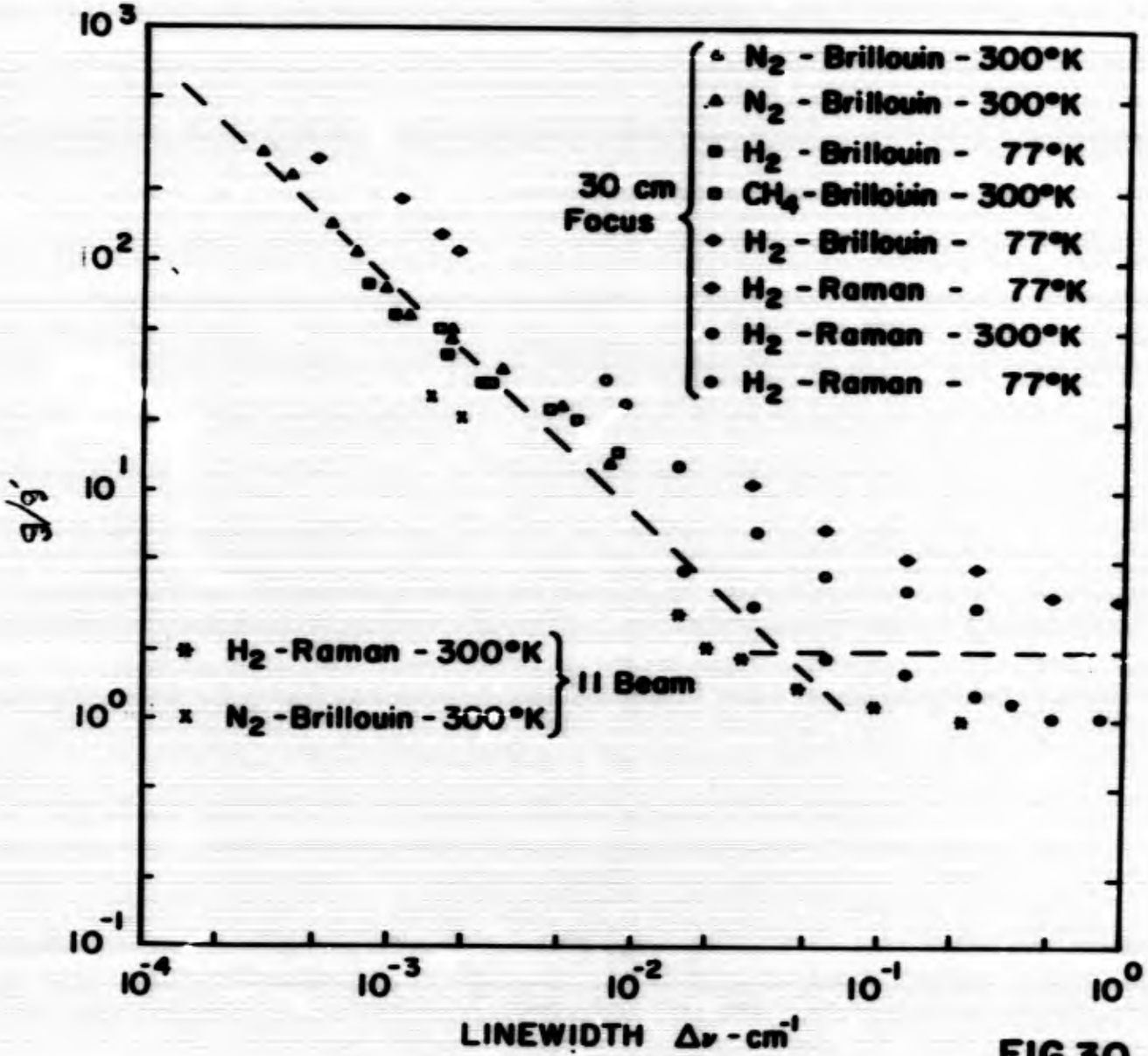
10^3
10^2
10^1
10^0
10^{-1}
g/g'
10^{-4}
10^{-3}
10^{-2}
10^{-1}
10^0
LINEWIDTH $\Delta\nu$ - cm^{-1}
N_2 - Brillouin - 300°K
N_2 - Brillouin - 300°K
H_2 - Brillouin - 77°K
CH_4 - Brillouin - 300°K
H_2 - Brillouin - 77°K
H_2 - Raman - 77°K
H_2 - Raman - 300°K
H_2 - Raman - 77°K
30 cm Focus
H_2 - Raman - 300°K
N_2 - Brillouin - 300°K
11 Beam

FIG.30

Accepting this time as real implies that the numerical calculations based on the simple theory are adequate to predict threshold powers for stimulated scattering in gases.

For these experiments several laser systems were used. A 1/4 x 2 inch ruby with a single Fresnel reflector produced a 3 to 10 MW output of excellent spatial properties. Adding a 3/4 x 9 inch not-so-good amplifier rod gave a 10-fold increase in power but only improved our ability to stimulate by a factor of 3. This smaller gain was likely due to the much poorer spatial quality of the amplified beam.

A double flat reflector has been used to mode select the 1/4 x 2 rod, usually giving a pair of lines separated by about 3/4 cm^{-1}, each line being about .005 cm^{-1} wide. More recently, the 5 MW output beam that can be conveniently obtained consists of a pair of equal intensity lines spaced by .008 cm^{-1}, each line probably being narrower than .003 cm^{-1}. The time response shows 4 nsec sine waves dipping to zero during each period. At other times, the depth of modulation is not as great.

REFERENCES

1) N. Bloembergen and Y. R. Shen, Phys. Rev. Letters 13, 720 (1964). P. L. Lallemand and N. Bloembergen, Appl. Phys. Letters 6, 210 and 6, 212 (1965).

2) N. M. Kroll, J. Appl. Phys. 36, 34 (1965).

3) R. Y. Chiao, E. Garmire, C. H. Townes, Phys. Rev. Letters 13, 479 (1964). G. Bret and G. Mayer, Compt. Rend. 258, 3265 (1964). P. L. Kelley, Phys. Rev. Letters 15, 1005 (1965).

4) Hagenlocker, Minck and Rado, to be published.

5) E. E. Hagenlocker and W. G. Rado, Appl. Phys. Letters 7, 236 (1965).

6) C. Trusdell, J. Rotational Mechanics Analysis 2, 643 (1953).

7) R. Y. Chiao, C. H. Townes, and B. P. Stoicheff, Phys. Rev. Letters 12, 592 (1964).

8) Nonlinear Optics, N. Bloembergen, W. A. Benjamin, Inc., New York (1965).

9) P. D. Maker and R. W. Terhune, Phys. Rev. 137, 801 (1965).

10) J. A. Armstrong, N. Bloembergen, J. Ducuing, P. S. Pershan, Phys. Rev. 127, 1918 (1962).

11) H. Takuma and D. A. Jennings, Appl. Phys. Letters 4, 185 (1964) and 5, 239 (1964). D. P. Bortfeld, W. R. Sooy, Appl. Phys. Letters 7, 283 (1965).

12) Martin Greenspan, J. Acoust. Soc. Am. 28, 644 (1956).

13) Spectra of Diatomic Molecules, G. Herzberg, D. Van Nostrand Co., Princeton, New Jersey, (1959).

14) C. H. Church, Univ. of Mich. Res. Inst. Techn. Rep. #1 (Jan. 1959) (ASTIA AD 211 110).

15) R. H. Dicke, Phys. Rev. 89, 472 (1953); J. P. Wittke and R. H. Dicke, Phys. Rev. 103, 620 (1956).

REFERENCES (Cont'd.)

16) Louis Galatry, Phys. Rev. 122, 1218 (1961).

17) S. Chandrasekhar, Rev. Mod. Phys. 15, 1 (1943).

18) Microwave Spectroscopy, C. H. Townes, McGraw Hill, New York, 1955.

19) Table of Thermodynamic and Transport Properties, J. Hilsenrath, Pergamon Press, New York 1960.

FIGURE CAPTIONS

1. Raman line strength per molecule - H_2. Data from: C. H. Church[14].
2. Raman line strength per molecule - D_2. Data from: C. H. Church[14].
3. Raman line strength per molecule - N_2. Data from: E. J. Stansbury, et al., Can. J. of Phys. 31, 954 (1953).
4. Raman line strength per molecule - O_2. Data from: E. J. Stansbury, ibid.
5. Raman linewidth for forward scattering H_2 - $Q_{01}(1)$.
   Data from: A. D. May et al., Can. J. Phys. 39, 1769 (1961).
6. Raman linewidth for forward scattering H_2 - $S_{00}(0)$.
   Data from: A. D. May, ibid.
7. Raman linewidth for forward scattering H_2 - $S_{00}(1)$.
   Data from: A. D. May, ibid.
8. Raman linewidth for forward scattering N_2 - $Q_{01}(J)$.
   Data from: G. R. Bird, J. Chem. Phys. 38, 2678 (1963).
9. Raman linewidth for forward scattering N_2 - $S_{00}(6)$.
   Data from G. R. Bird, ibid.
10. Raman linewidth for forward scattering N_2 - $S_{00}(8)$.
    Data from G. R. Bird, ibid.
11. Raman linewidth for forward scattering O_2 - $S_{00}(11)$.
    Data from G. R. Bird, ibid.
12. Normalized gain factor for stimulated Raman in H_2 - $Q_{01}(1)$.
13. Normalized gain factor for stimulated Raman in H_2 - $S_{00}(0)$.
14. Normalized gain factor for stimulated Raman in H_2 - $S_{00}(1)$.
15. Normalized gain factor for stimulated Raman in N_2 - $Q_{01}(6)$.

FIGURE CAPTIONS (Cont'd.)

16. Normalized gain factor for stimulated Raman in N_2 - $S_{00}(6)$.
17. Normalized gain factor for stimulated Raman in N_2 - $S_{00}(8)$.
18. Normalized gain factor for stimulated Raman in O_2 - $S_{00}(11)$.
19. Brillouin linewidth in H_2. Dashed lines indicate high loss region where model becomes uncertain.
20. Brillouin linewidth in D_2. Dashed lines indicate high loss region where model becomes uncertain.
21. Brillouin linewidth in N_2. Dashed lines indicate high loss region where model becomes uncertain.
22. Brillouin linewidth in O_2. Dashed lines indicate high loss region where model becomes uncertain.
23. Normalized gain factor for stimulated Brillouin in H_2.
24. Normalized gain factor for stimulated Brillouin in D_2.
25. Normalized gain factor for stimulated Brillouin in N_2.
26. Normalized gain factor for stimulated Brillouin in O_2.
27. Calculated normalized power gain for sbs and srs in H_2 at 300°K. The right ordinate scale for inverse threshold power was adjusted by a constant factor to fit the data to the transient raman gain curve at the high pressures. A time of 2 nsec was used. (See text)
28. Calculated normalized power gain for sbs and srs in N_2 at 300°K. The right ordinate scale for inverse threshold power was adjusted by a constant factor to fit the data to the transient brillouin gain curve at the low pressures. A time of 2 nsec was used. (See text)

FIGURE CAPTIONS (Cont'd.)

29. Calculated normalized power gain for sbs and srs in H_2 at 77°K. Both processes exhibited threshold behavior even though both were occurring simultaneously. The right ordinate scale for inverse threshold power was adjusted by a single constant factor to fit the srs data at high pressures to the transient gain curves. A time of 2 nsec was used. (See text)

30. Ratio of calculated to experimental gain as a function of transition linewidth. The experimental gain value was calculated from the threshold power using $\ell/A = 5n/\lambda$ for a focus. Data, assembled for both srs and sbs in a variety of materials, at several temperatures, with different laser systems, and involving both focused and parallel beams, all fall close to a curve which implies a 2 nsec transient behavior. (See text)

TABLE CAPTIONS

Table 1. Approximate raman transition frequencies

2. Raman transition frequencies in H_2

3. Raman transition frequencies in D_2

4. Raman transition frequencies in N_2

5. Raman transition frequencies in O_2

6. Population distribution among rotational levels in H_2

7. Population distribution among rotational levels in D_2

8. Population distribution among rotational levels in N_2

9. Population distribution among rotational levels in O_2

10. Raman scattering intensities. $\alpha_{vv'}$ and $\gamma_{vv'}$ are the isotropic and anisotropic raman polarizabilities for transitions involving the v and v′ vibrational levels.